J. Fluid Mech. (2006), *vol.* 548, *pp.* 309–340.
doi:10.1017/S0022112005007731 Printed in the United Kingdom

Linear and nonlinear analysis of shallow wakes

By M. S. GHIDAOUI[1], A. A. KOLYSHKIN[1], J. H. LIANG[1], F. C. CHAN[1], Q. LI[1] AND K. XU[2]

[1]Department of Civil Engineering, The Hong Kong University of Science and Technology, Kowloon, Hong Kong

[2]Department of Mathematics, The Hong Kong University of Science and Technology, Kowloon, Hong Kong

(Received 28 August 2003 and in revised form 5 August 2005)

The bottom friction and the limited vertical extent of the water depth play a significant role in the dynamics of shallow wakes. These effects along with the effect of the strength of the shear layer define the wake parameter S. A nonlinear model, based on a second-order explicit finite volume solution of the depth-averaged shallow water equation in which the fluxes are obtained from the solution of the Bhatnagar–Gross–Krook (BGK) Boltzmann equation, is developed and applied to shallow wake flows for which laboratory data are available. The velocity profiles, size of the recirculating wake, oscillation frequency, and wake centreline velocity are studied. The computed and measured results are in reasonable agreement for the vortex street (VS) and unsteady bubble (UB) regimes, but not for the steady bubble (SB). The computed length of the recirculation region is about 60 % shorter than the measured value when S belongs to the SB regime. As a result, the stability investigation performed in this paper is restricted to S values away from the transition between SB and UB. Linear analysis of the VS time-averaged velocity profiles reveals a region of absolute instability in the vicinity of the cylinder associated with large velocity deficit, followed by a region of convective instability, which is in turn followed by a stable region. The frequency obtained from Koch's criterion is in good agreement with the shedding frequency of the fully developed VS. However, this analysis does not reveal the mechanism that sets the global shedding frequency of the VS regime because the basic state is obtained from the VS regime itself. The mechanism responsible for VS shedding is sought by investigating the stability behaviour of velocity profiles in the UB regime as S is decreased towards the critical value which defines the transition from the UB to the VS. The results show that the near wake consists of a region of absolute instability sandwiched between two convectively unstable regions. The frequency of the VS appears to be predicted well by the selection criteria given in Pier & Huerre (2001) and Pier (2002), suggesting that the 'wave-maker' mechanism proposed in Pier & Huerre (2001) in the context of deep wakes remains valid for shallow wakes. The amplitude spectra produced by the nonlinear model are characterized by a narrow band of large-amplitude frequencies and a wide band of small-amplitude frequencies. Weakly nonlinear analysis indicates that the small amplitude frequencies are due to secondary instabilities. Both the UB and VS regimes are found to be insensitive to random forcing at the inflow boundary. The insensitivity to random noise is consistent with the linear results which show that the UB and VS flows contain regions of absolute instabilities in the near wake where the velocity deficit is large.

1. Introduction

Turbulent shallow flows such as jets, mixing layers and wakes are common in nature. Such flows are observed in rivers, estuaries, compound and composite channels, and oceans as well as in the atmosphere. In this paper we analyse shallow wakes, that is, flows behind obstacles (such as islands and headlands) in a shallow environment. Shallow flow models are used where the transverse length scale of the flow is much larger than the vertical length scale. In this case the system of Navier–Stokes equations is integrated with respect to the vertical length scale. Using the hydrostatic approximation for the pressure one then obtains a system of shallow water equations which is widely used in the analysis of such flows. Field, laboratory and numerical data show the existence of quasi-two-dimensional coherent structures in shallow flows. In a recent paper, Jirka (2001) formulated four basic approaches which are used to study coherent structures in shallow flows: field data, experimental analysis, numerical experiments and stability analysis. Aerial photographs and satellite images show different flow patterns behind islands and around mountains (Wolanski, Imberger & Heron 1984; Ingram & Chu 1987). Photograph number 173 in Van Dyke (1982) shows the development of shallow wakes in the lee of the leaking tanker Argo Merchant. Despite the fact that the Reynolds number of the flow is quite high, the flow pattern closely resembles the well-known von Kármán vortex street pattern small Reynolds numbers.

Shallow mixing layers were studied experimentally by Chu & Babarutsi (1988), Uijttewaal & Booij (2000), van Prooijen & Uijttewaal (2002). Turbulent shallow wakes are analysed in the experiments of Chen & Jirka (1995), Balachandar, Tachie & Chu (1999), Balachandar, Ramachandran & Tachie (2000), Tachie & Balachandar (2001). It is found in these studies that the shallowness of fluid layer plays an important role in the development of the wake. In particular, the wake momentum defect is reduced by the bed friction force, which will eventually nullify the wake in the far region. Different flow patterns observed in the experiments by Chen & Jirka (1995) were classified using the stability parameter $S = c_f D/h$, where c_f is the friction coefficient, D is the characteristic length scale of the obstacle (in the experiments of Chen & Jirka (1995) D was the diameter of a cylinder or the width of a plate) and h is water depth. The stability parameter S was introduced earlier, in the paper by Ingram & Chu (1987). The structures observed for small S (of order 0.2 or less) closely resemble the classical vortex street (VS) pattern known for flows in deep water for small Reynolds numbers. For larger S (approximately from 0.2 to 0.5) the wake consists of two counter-rotating eddies which oscillate in the cross-stream direction followed by a sinuous tail. Such a flow pattern is referred to as an unsteady bubble (UB). Finally, if the stability parameter S is larger than about 0.6, the wake consists of two non-oscillatory counter-rotating eddies with no visible oscillations downstream. This flow pattern is referred to as steady bubble (SB).

Coherent structures that are observed in shallow wakes are believed to appear as a result of flow instability. Methods of hydrodynamic stability theory were used by Chu, Wu & Khayat (1983, 1991), Grubišič, Smith & Schär (1995), Chen & Jirka (1997, 1998), Ghidaoui & Kolyshkin (1999), van Prooijen & Uijttewaal (2002), Kolyshkin & Ghidaoui (2002, 2003), Socolofsky, von Carmer & Jirka (2003) in an attempt to describe the behaviour of flows in shallow water. Several conclusions can be drawn from the results of stability analysis. First, the validity of the rigid-lid assumption is assessed. It is shown in Ghidaoui & Kolyshkin (1999) that the error in the determination of the critical values of the stability parameter S is about 10–15 % if the Froude number of the flow (based on water depth) does not exceed 0.6. The use of the rigid-lid assumption allows one to simplify the shallow water equations and reduce

them to one equation for the stream function, as is usually done in two-dimensional hydrodynamics. Second, different patterns observed in shallow wakes (vortex street, unsteady bubble, steady bubble) are classified in Chen & Jirka (1997) using the concepts of stable, convectively unstable and absolutely unstable flows. Reasonable agreement is found between theoretical predictions from the linear stability analysis and experimental data in Chen & Jirka (1997) and Socolofsky *et al.* (2003) for shallow wakes and in van Prooijen & Uijttewaal (2002) for shallow mixing layers. Third, it is shown in Kolyshkin & Ghidaoui (2003) that if the stability parameter S is slightly below the critical value then the evolution of the most unstable mode is governed by a complex Ginzburg–Landau equation. Satisfactory agreement is found between the results of nonlinear simulation in Grubišič *et al.* (1995) and the Ginzburg–Landau model in terms of the wake saturation amplitude.

Numerical investigation of turbulent shallow wakes was performed by Lloyd & Stansby (1997*a*, *b*), Stansby & Lloyd (2001) and Stansby (2003). Lloyd & Stansby (1997*a*, *b*) investigated steady ambient flows around conical islands of small slope both experimentally and numerically. Oscillatory ambient flows around islands of small slope were analysed by Stansby & Lloyd (2001). Stansby (2003) describes a mixing-length model for shallow turbulent wakes where the vertical length scale is assumed to be proportional to the horizontal length scale. The coefficient of proportionality is found from the comparison with experimental data.

Previous studies of shallow wake flows indicate that a more detailed picture of the flow can be obtained if several methods of analysis are combined (for example, linear stability analysis and experimental modelling as in Chen & Jirka (1997), numerical modelling and experimental analysis as in Lloyd & Stansby (1997*a*, *b*). In the present paper we analyse shallow wake flows using the methods of linear and weakly nonlinear theory as well as numerical integration of full two-dimensional shallow water equations.

2. Governing equations

The problem under investigation consists of a free-surface water flow around an island. The mass and momentum equations for an incompressible homogeneous viscous fluid flow such as that around islands are (Schlichting 1979; Hinze 1987; Pope 2000)

$$\frac{\partial u_\alpha}{\partial x_\alpha} + \frac{\partial w}{\partial z} = 0, \tag{2.1}$$

$$\frac{\partial u_\alpha}{\partial t} + \frac{\partial u_\kappa u_\alpha}{\partial x_\kappa} + \frac{\partial w u_\alpha}{\partial z} = -\frac{1}{\rho}\frac{\partial p}{\partial x_\alpha} + \nu\frac{\partial^2 u_\alpha}{\partial x_\kappa \partial x_\kappa} + \nu\frac{\partial^2 u_\alpha}{\partial z^2}, \tag{2.2}$$

$$\frac{\partial w}{\partial t} + \frac{\partial u_\kappa w}{\partial x_\kappa} + \frac{\partial w^2}{\partial z} = -g - \frac{1}{\rho}\frac{\partial p}{\partial z} + \nu\frac{\partial^2 w}{\partial x_\kappa \partial x_\kappa} + \nu\frac{\partial^2 w}{\partial z^2}, \tag{2.3}$$

where g is the gravitational acceleration; ρ is the density of the fluid (water); t is time; $\kappa = 1, 2$ and $\alpha = 1, 2$ with 1 indicating the streamwise direction and 2 indicating the cross-stream direction; $(x_\alpha, z) = (x_1, x_2, z)$ are the streamwise, cross-stream and vertical coordinates, respectively; $(u_\alpha, w) = (u_1, u_2, w)$ are the velocities in directions (x_1, x_2, z), respectively; p is the pressure; and ν is the kinematic viscosity of the fluid (water).

Let

$$\bar{\phi}(x_\alpha, z, t) = \int_{-\infty}^{\infty}\int_{-\infty}^{\infty}\int_{-\infty}^{\infty} \phi(x'_\alpha, z', t) G(x'_\alpha - x_\alpha, z' - z, t)\,\mathrm{d}x_1\,\mathrm{d}x_2\,\mathrm{d}z,$$

where $\bar{\phi}$ is the filtered (resolvable) part of ϕ; and G is a function which is a characteristic of the filter. Applying the filtering operation to (2.1), (2.2) and (2.3) gives (Pope 2000)

$$\frac{\partial \bar{u}_\alpha}{\partial x_\alpha} + \frac{\partial \bar{w}}{\partial z} = 0, \tag{2.4}$$

$$\frac{\partial \bar{u}_\alpha}{\partial t} + \frac{\partial \bar{u}_\kappa \bar{u}_\alpha}{\partial x_\kappa} + \frac{\partial \bar{w}\bar{u}_\alpha}{\partial z} = -\frac{1}{\rho}\frac{\partial \bar{p}}{\partial x_\alpha} + \nu\frac{\partial^2 \bar{u}_\alpha}{\partial x_\kappa \partial x_\kappa} + \nu\frac{\partial^2 \bar{u}_\alpha}{\partial z^2} + \frac{\partial(\bar{u}_\kappa \bar{u}_\alpha - \overline{u_\kappa u_\alpha})}{\partial x_\kappa} + \frac{\partial(\bar{w}\bar{u}_\alpha - \overline{w u_\alpha})}{\partial z}, \tag{2.5}$$

$$\frac{\partial \bar{w}}{\partial t} + \frac{\partial \bar{u}_\kappa \bar{w}}{\partial x_\kappa} + \frac{\partial \bar{w}^2}{\partial z} = -g - \frac{1}{\rho}\frac{\partial \bar{p}}{\partial z} + \nu\frac{\partial^2 \bar{w}}{\partial x_\kappa \partial x_\kappa} + \nu\frac{\partial^2 \bar{w}}{\partial z^2} + \frac{\partial(\bar{u}_\kappa \bar{w} - \overline{u_\kappa w})}{\partial x_\kappa} + \frac{\partial(\bar{w}^2 - \overline{w^2})}{\partial z}. \tag{2.6}$$

The last terms on the right-hand side of (2.5) and (2.6) represent the momentum exchange between the resolved and unresolved scales of motion.

The use of linear and nonlinear analyses to investigate the emergence and evolution of large-scale coherent structures in the wake of islands is of a particular interest in this study. The horizontal and vertical length and velocity scales of these coherent structures are given by (L_X, U) and (L_Z, W), respectively. In the vicinity of the island, L_X is of a similar order of magnitude to the island diameter D. Further downstream, the coherent structures may undergo pairing as well as spreading with the result being that L_X may exceed D. Therefore, $L_X \geqslant O(D)$, where O is the order of magnitude operator as defined in Pedlosky (1987). The vertical length scale, L_Z, of the coherent structures is constrained by the water depth, where L_Z is generally much smaller than D and L_X (i.e. $L_Z/L_X \ll 1$). Very far from the island, however, the coherent structures are annihilated by the bottom friction.

Considering flows with $L_Z/L_X \ll 1$, the vertical momentum equation reduces to a balance between gravity and pressure gradient (i.e. hydrostatic pressure distribution). Using the hydrostatic distribution and integrating (2.4) and (2.5) with respect to water depth, h, gives the following shallow water equations:

$$\frac{\partial \bar{h}}{\partial t} + \frac{\partial \bar{h}\bar{\hat{u}}_\alpha}{\partial x_\alpha} = 0, \tag{2.7}$$

$$\frac{\partial \bar{h}\bar{\hat{u}}_\alpha}{\partial t} + \frac{\partial \bar{h}\bar{\hat{u}}_\kappa \bar{\hat{u}}_\alpha + \delta_{\kappa\alpha} g\bar{h}^2/2}{\partial x_\kappa} = g\bar{h}S_{0_\alpha} - \frac{\bar{\tau}_{b_\alpha}}{\rho} + \nu\frac{\partial}{\partial x_\kappa}\left(\bar{h}\frac{\partial \bar{\hat{u}}_\alpha}{\partial x_\kappa}\right) + \frac{\partial \bar{h}(\bar{\hat{u}}_\kappa \bar{\hat{u}}_\alpha - \widehat{\overline{u_\kappa u_\alpha}})}{\partial x_\kappa}, \tag{2.8}$$

where the hat denotes the depth-averaging operator; $\delta_{\kappa\alpha} = 1$ when $\kappa = \alpha$ and 0 otherwise; $b(x_\alpha)$ is the vertical distance from an arbitrary datum defined by $z = 0$ to the bed of the channel, river, lake or ocean; $S_{0_\alpha} = \partial b/\partial x_\alpha$ are the slopes of the flow bed along x_1 and x_2; and $\bar{\tau}_{b_\alpha} = -\mu\partial\bar{u}_\alpha/\partial z$ at $z = b$ are the shear stresses at the bed of the flow along x_1 and x_2. Note that the shallow flows being investigated are characterized by small values of surface water and bed slopes. Therefore, the filter function G is separable, leading to $\hat{\bar{\phi}} = \bar{\hat{\phi}}$ (Hinterberger, Frohlich & Rodi 2003). This result has been used in the derivation of (2.7) and (2.8). These equations are not closed because $\bar{\tau}_{b_\alpha}$ and $\widehat{\overline{u_\kappa u_\alpha}}$ are unknown. The turbulent stresses can be estimated from the following turbulence closure model:

$$\nu_e = l_m^2\sqrt{2S_{\kappa\alpha}S_{\kappa\alpha}}, \quad S_{\kappa\alpha} = \frac{1}{2}\left(\frac{\partial \bar{\hat{u}}_\alpha}{\partial x_\kappa} + \frac{\partial \bar{\hat{u}}_\kappa}{\partial x_\alpha}\right), \tag{2.9}$$

where ν_e is eddy viscosity. Although there is no theoretical foundation for applying the Smagrorinsky model to two-dimensional flows, the adoption of this model outside its domain of applicability has generally led to encouraging results. For example, the model adopted in this paper has been successfully applied by Zhou (2004) to channel flows as well as conical-island shallow wake flows. In addition, the Princeton Ocean Model (POM) uses the Smagorinsky relation to estimate the horizontal component of the turbulent diffusion (Mellor 2004). The POM model has been successfully applied to a wide range of problems in ocean circulations (e.g. Oey, Ezer & Lee 2005). It is worthwhile noting that the two-dimensional version of the Smagorinsky model belongs to the general class of mixing-length models (Pope 2000), where the mixing length is related to the grid size by the van Driest formula: $l_m = \sqrt{\Delta x \Delta y}[1 - \exp(-r^+/A)]/C_s^2$, where C_s is the Smagorinsky constant; $r^+ = u_*(r - D/2)/\nu$ is the dimensionless radial distance from the island; $D/2$ is the island diameter and u_* is the shear velocity. The van Driest formula ensures that the eddy viscosity becomes zero in the viscous sublayer.

The shear stresses at the bed of the flow are modelled using the following quadratic friction law (Schlichting 1979; Hinze 1987; Pope 2000):

$$\tau_{b_\alpha} = \tfrac{1}{2}\rho c_f \bar{u}_\alpha \sqrt{\bar{u}_\kappa \bar{u}_\kappa}, \tag{2.10}$$

where c_f is the friction coefficient. The $1/2$ in (2.10) is adopted for consistency with the work of Chen & Jirka (1997). Other papers and textbooks may drop the $1/2$ and, therefore, their friction coefficient would be half the one used in this paper. Hence, care is needed when one is comparing results from different authors. The friction coefficient for the case of a smooth bed is given by the semi-empirical quadratic friction law (Schlichting 1979; Hinze 1987; Pope 2000):

$$\frac{1}{\sqrt{c_f}} = -4\log\left(\frac{1.25}{4Re\sqrt{c_f}}\right), \tag{2.11}$$

where $Re = UL_Z/\nu$ is the Reynolds number and ν is the dynamic viscosity of the fluid. The resistance coefficient of a rough surface depends on both Re and the relative roughness coefficient k_s of the surface (Schlichting 1979; Hinze 1987; Pope 2000) and can be obtained by Colebrook–White formula:

$$c_f = \frac{1}{16}\left[\log\left(\frac{k_s/h}{3.71} + \frac{5.74}{Re^{0.9}}\right)\right]^{-2}. \tag{2.12}$$

The resistance coefficient for a laminar flow varies as the inverse of the Reynolds number.

3. Numerical method

The system (2.7), (2.8) and (2.10) is solved using a conservative finite volume on irregular grids, where the algorithm for the mass and momentum fluxes at the control surface of the finite volume is obtained from the solution of the Bhatnagar–Gross–Krook (BGK) Boltzmann equation. The scheme is explicit and second order in both time and space. The spatial variation of flow velocity and water depth within a cell is obtained using a second-order nonlinear limiter. A summary of the BGK scheme is provided in this section. Detailed derivation and an in-depth analysis of the BGK model for shallow water flows can be found in Ghidaoui *et al.* (2001) and Liang *et al.* (2005).

The BGK scheme has its roots in the idea that the shallow water equations are obtainable as moments of a Boltzmann-like equation. In particular, the BGK equation for shallow flows is (Ghidaoui *et al.* 2001; Xu 2002)

$$\frac{\partial f}{\partial t} + c_\alpha \frac{\partial f}{\partial x_\alpha} + \left(S_{0_\alpha} - c_f \bar{\hat{u}}_\alpha \sqrt{\bar{\hat{u}}_\kappa \bar{\hat{u}}_\kappa}/\bar{h}\right) \frac{\partial f}{\partial c_\alpha} = \frac{f_e - f}{t_c} \tag{3.1}$$

where

$$f_e(x_\alpha, c_\alpha, t) = \frac{1}{\pi g} \exp\left[-\frac{(c_\alpha - v_\alpha)(c_\alpha - v_\alpha)}{g\bar{h}}\right] \tag{3.2}$$

and c_α is random particle speed along x_α, f is the distribution function of c_α, and t_c is the relaxation time to be defined later in this section. The distribution function satisfies the following relations:

$$\begin{bmatrix} \bar{h} \\ \bar{h}\bar{\hat{u}}_\alpha \\ \bar{h}\bar{\hat{u}}_\kappa \bar{\hat{u}}_\alpha + \delta_{\kappa\alpha}\bar{h}^2/2 - t_c g \bar{h}\bar{h}\left(\dfrac{\partial \bar{\hat{u}}_\alpha}{\partial x_\kappa} + \dfrac{\partial \bar{\hat{u}}_\kappa}{\partial x_\alpha}\right) \end{bmatrix} = \int_{-\infty}^{\infty}\int_{-\infty}^{\infty} \begin{bmatrix} 1 \\ c_\alpha \\ c_\kappa c_\alpha \end{bmatrix} f \, \mathrm{d}c_x \, \mathrm{d}c_z. \tag{3.3}$$

The zeroth and first moments of (3.1) with respect to c_α are

$$\frac{\partial \bar{h}}{\partial t} + \frac{\partial \bar{h}\bar{\hat{u}}_\alpha}{\partial x_\alpha} = 0, \tag{3.4}$$

$$\frac{\partial \bar{h}\bar{\hat{u}}_\alpha}{\partial t} + \frac{\partial \bar{h}\bar{\hat{u}}_\kappa \bar{\hat{u}}_\alpha + \delta_{\kappa\alpha}\bar{h}^2/2}{\partial x_\kappa} = \bar{h} S_{0_\alpha} - c_f \bar{\hat{u}}_\alpha \sqrt{\bar{\hat{u}}_\kappa \bar{\hat{u}}_\kappa} + \frac{\partial (t_c g \bar{h})\bar{h}}{\partial x_\kappa} \frac{\partial \bar{\hat{u}}_\alpha}{\partial x_\kappa}. \tag{3.5}$$

Note that system (3.4)–(3.5) is identical to (2.7) and (2.8) if $t_c g\bar{h} = \nu + (\bar{\hat{u}}_\kappa \bar{\hat{u}}_\alpha - \widehat{\overline{u_\kappa u_\alpha}})/\partial\bar{\hat{u}}_\alpha/\partial x_\kappa$. This connection between the BGK model and the shallow water equation is exploited to formulate a numerical scheme for (2.7) and (2.8) on the basis of the BGK equation.

Let Ω be the flow domain. This flow domain is divided into $I \times J$ cells (control volumes) of arbitrary shapes, Ω_{ij} with $i = 1 \ldots I$ and $j = 1 \ldots J$, such that $\Omega = \cup\Omega_{ij}$. Here i and j denote the spatial index along the x_1 and x_2 coordinates, respectively. The time domain is divided into N equal intervals. The length of each time interval is Δt and the kth time level denotes $t = k\Delta t$. Integration of (3.4)–(3.5) over Ω_{ij} from k to $k+1$ gives

$$\boldsymbol{U}_{ij}^{k+1} = \boldsymbol{U}_{ij}^{k} - \frac{1}{\Omega_{ij}} \oint_{\partial\Omega_{ij}} \int_k^{k+1} (\boldsymbol{F} + \boldsymbol{F}_{t_c}) \cdot \boldsymbol{n} \, \mathrm{d}t \, \mathrm{d}l + \frac{1}{\Omega_{ij}} \int_{\Omega_{ij}} \int_k^{k+1} \boldsymbol{B} \, \mathrm{d}t \, \mathrm{d}x_1 \, \mathrm{d}x_2, \tag{3.6}$$

where

$$\boldsymbol{U} = \begin{bmatrix} \bar{h} \\ \bar{h}\bar{\hat{u}}_\alpha \end{bmatrix},$$

$$\boldsymbol{F} + \boldsymbol{F}_{t_c} = \begin{bmatrix} \bar{h}\bar{\hat{u}}_\alpha \\ \bar{h}\bar{\hat{u}}_\kappa \bar{\hat{u}}_\alpha + \delta_{\kappa\alpha}\bar{h}^2/2 - \tau g \bar{h}\bar{h}\left(\dfrac{\partial \bar{\hat{u}}_\alpha}{\partial x_\kappa} + \dfrac{\partial \bar{\hat{u}}_\kappa}{\partial x_\alpha}\right) \end{bmatrix},$$

$$\boldsymbol{B} = \begin{bmatrix} 0 \\ \bar{h} S_{0_\alpha} - c_f \bar{\hat{u}}_\alpha \sqrt{\bar{\hat{u}}_\kappa \bar{\hat{u}}_\kappa} \end{bmatrix},$$

and where $\boldsymbol{n} = (\mathrm{d}y\boldsymbol{i} - \mathrm{d}x\boldsymbol{j})/\mathrm{d}l$ is the local unit outward vector normal to $\partial\Omega_{ij}$; $\boldsymbol{t} = (\mathrm{d}x\boldsymbol{i} + \mathrm{d}y\boldsymbol{j})/\mathrm{d}l$ is the unit tangent vector to the surface when going around the boundary in the counter-clockwise direction, and $\mathrm{d}l = \sqrt{\mathrm{d}x^2 + \mathrm{d}y^2}$.

An algorithm for the unknown flux term on the right-hand side of (3.6) is required. Traditional approaches use upwind schemes such as the Riemann solution to estimate the flux associated with $\boldsymbol{F}$ and central differencing to estimate the flux associated with $\boldsymbol{F}_\tau$. The BGK scheme uses the connection between the Boltzmann distribution and the Boltzmann equation to determine this flux term. In particular, note that $\boldsymbol{F} + \boldsymbol{F}_{t_c}$ represent the second and third rows of (3.3). The relation between $\boldsymbol{F} + \boldsymbol{F}_{t_c}$ and f means that one can develop an algorithm for $\boldsymbol{F} + \boldsymbol{F}_{t_c}$ by approximating f using the BGK equation and inserting the result into the second and third rows of (3.3). A second-order solution in time and space of (3.1) at a cell boundary is (Ghidaoui *et al.* 2001)

$$f(t, x_\alpha) = \gamma_1 f_e^k(x_\alpha) + \gamma_2 f_e^k(x_\alpha^+) + \gamma_3 f_e^k(x_\alpha^-), \tag{3.7}$$

where $t \in [k\Delta t, (k+1)\Delta t]$; $x_\alpha \in \partial\Omega_{ij}$; x_α^+ tends to x_α from the outside of Ω_{ij}; x_α^- tends to $x_\alpha \in \partial\Omega_{ij}$ from the inside of Ω_{ij}; and $(\gamma_1, \gamma_1, \gamma_2)$ are known functions of time and particle speeds (Ghidaoui *et al.* 2001). The algorithm for the net flux from cell Ω_{ij} is

$$\boldsymbol{F} + \boldsymbol{F}_{t_c} = \int_{-\infty}^{\infty}\int_{-\infty}^{\infty} \begin{bmatrix} 1 \\ c_\alpha \\ c_\kappa c_\alpha \end{bmatrix} \left(\gamma_1 f_e^k(x_\alpha) + \gamma_2 f_e^k(x_\alpha^+) + \gamma_3 f_e^k(x_\alpha^-)\right) \mathrm{d}c_{x_1}\, \mathrm{d}c_{x_2}. \tag{3.8}$$

The integration in (3.8) is carried out analytically because all the moments of the Gaussian distribution, f_e, are known. The explicit form of the net flux is given in the Appendix.

The current BGK model has been previously tested for a wide range of shallow water flows. For example, Ghidaoui *et al.* (2001) demonstrated the accuracy and efficiency of the BGK scheme by applying it to (i) strong shock waves, (ii) extreme expansion waves, (iii) a combination of strong shock waves and extreme expansion waves and (iv) one- and two-dimensional dam break problems. In addition, Xu (2002) developed a well-balanced BGK scheme for the shallow water equations with source terms. Moreover, Liang *et al.* (2005) showed that BGK model couples both wave and diffusion very well without operator splitting. It should also be noted that Boltzmann-based schemes have been developed and applied to a multitude of hydrodynamic problems such as shock waves in compressible flows (e.g. Reitz 1981; Xu 2001), multicomponent and multiphase flows (e.g. Gunstenson *et al.* 1991; Xu 1997*a*), flows in complex geometries (e.g. Rothman 1988; Chen & Doolen 1998), turbulent flows (e.g. Chen, Chen & Matthaeus 1992; Zhou 2004), low Mach number flows (e.g. Su, Xu & Ghidaoui 1999), and heat transfer and reaction diffusion flows (e.g. Xu 1997*b*).

Figure 1 shows a typical grid system, where the circle in the middle represents the island and the dimensionless distances are $x = x_1/L_X$ and $y = x_2/L_X$. The no-slip condition is used at the island and channel walls. The discharge is specified at the inflow boundary, while the water depth is specified at the downstream boundary. Several convergence tests are performed. As an example, the results of the simulation of the unsteady bubble case (CY43, see Chen & Jirka 1995) for different mesh sizes, namely, 240×75, 320×100, 400×125 and 480×150 are shown in table 1. The instantaneous longitudinal velocity $\bar{\hat{u}}_1$ is calculated at different locations x_1/D along the centreline at $t = 1000$ s. The results for different mesh sizes are compared to those of the finest mesh (480×150). No noticeable changes in the results were observed by

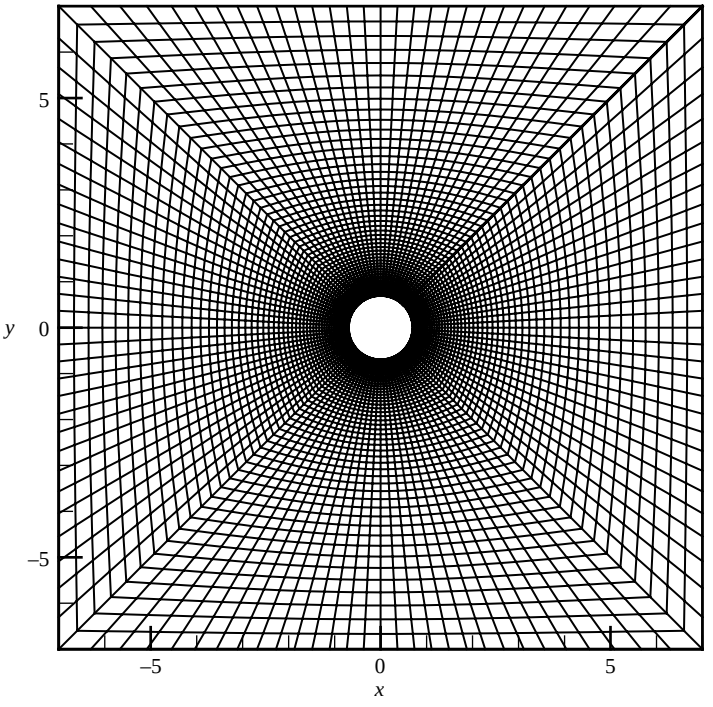

FIGURE 1. Computational grid.

x_1/D	480×150	240×74	% error
1.0	0.161253	0.162690	0.89
2.0	0.158243	0.156699	−0.98
3.0	0.163090	0.162768	−0.20
x_1/D	480×150	320×100	% error
1.0	0.161253	0.163035	1.11
2.0	0.158243	0.157741	−0.32
3.0	0.163090	0.162857	−0.14
x_1/D	480×150	400×125	% error
1.0	0.161253	0.162696	0.90
2.0	0.158243	0.158042	−0.13
3.0	0.163090	0.163061	−0.02

TABLE 1. Convergence test results.

further mesh refinement beyond (480×150). In general, the percentage error, which measures the difference between the results obtained from a coarse mesh and the results obtained by the finest mesh, show that the error is small and that this error becomes smaller as the number of grid points increases. Note that the error with a mesh size of 320×100 is of order 1%. Therefore, unless stated otherwise, this mesh is used for the nonlinear calculations presented in the paper. Figure 2 shows the convergence of the numerical solution as the number of grid points increases. The

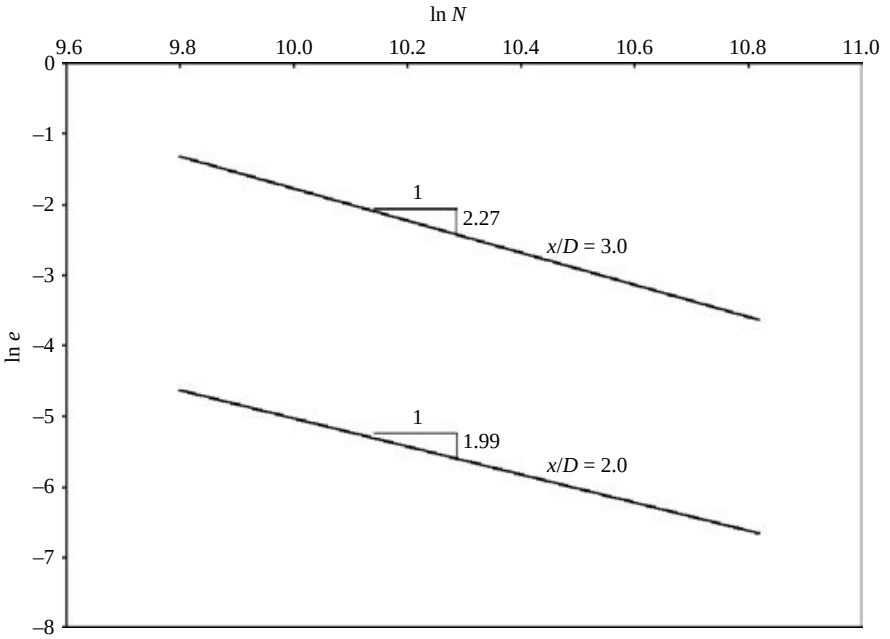

FIGURE 2. Convergence of the BGK scheme at two different locations downstream of the island.

slope of these curves is around 2, confirming that the overall order of the scheme is close to 2.

4. Range of validity of the depth-averaged equations

This section assesses the ability of the depth-averaged shallow water model to describe shallow wake flows. This is accomplished by applying the model to test rigs for which there are data available. The velocity profiles, wake size, shedding frequency and centreline velocity are compared.

Figure 3 shows the computed and measured time-averaged streamwise velocity profiles at different stations downstream of the island. The measured profiles are obtained from Socolofsky *et al.* (2003). The time-averaged profiles are calculated by the formula

$$U_{av}(X_1, X_2) = \frac{1}{T_0} \int_{T_s}^{T_f} U_1(X_1, X_2, T)\, \mathrm{d}T, \tag{4.1}$$

where T_s is the starting time of the averaging (which is assumed to be large enough to ensure that the transient time is smaller than T_s), T_f is the final time and $T_0 = T_f - T_s$. The values of T_s and T_f are 750 s and 4000 s, respectively. The magnitude of the return velocity and the gradient of the velocity deficit, which are important for flow stability, are represented well by the model. However, the magnitude of the computed velocity at the shoulders of the cylinder are slightly larger than the measured values. This is probably due to the fact that while the model gives depth-averaged profiles, the measured profiles are sampled at a particular water depth. There are no available measured depth-averaged profiles for shallow wakes.

Figure 4 shows the computed and measured Strouhal number St as a function of the parameter S, where $St = fD/U$ and f is the frequency of wake oscillation.

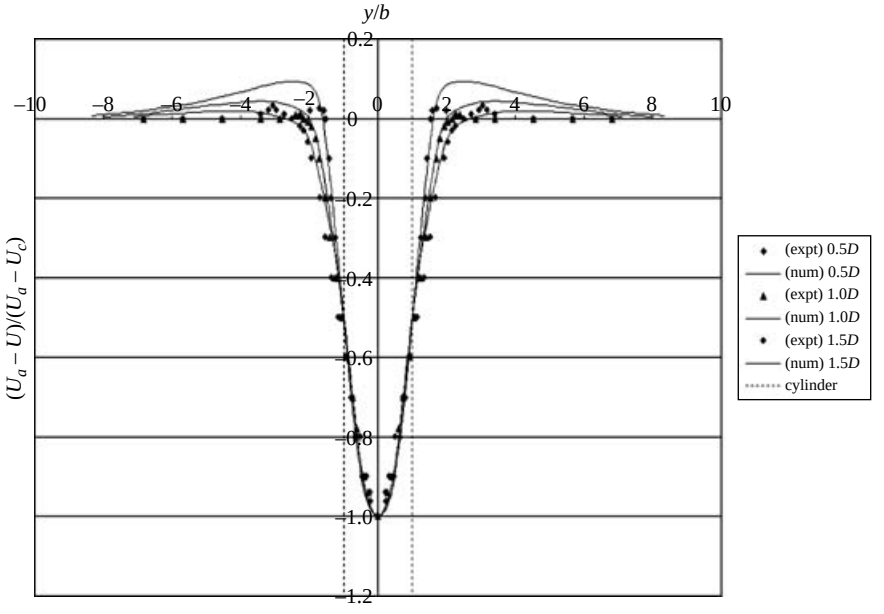

FIGURE 3. Comparison between measured and computed time-averaged mean flow in the x-direction.

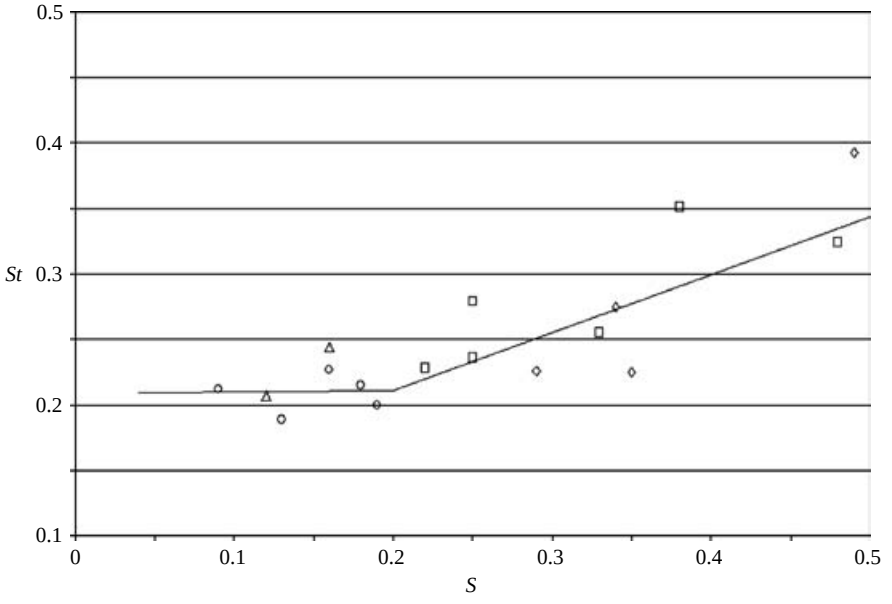

FIGURE 4. Strouhal number St as a function of the parameter S. Experimental points from Chen & Jirka (1995): circles for $S \leqslant 0.2$ (i.e. VS case); and squares for $0.2 \leqslant S \leqslant 0.5$ (i.e. UB case). Calculated points: triangles for $S \leqslant 0.2$; diamonds for $0.2 \leqslant S \leqslant 0.5$; and stars for $S \geqslant 0.5$.

The computed and measured shedding frequencies are in reasonable agreement over a wide range of the stability parameter. This suggests that mechanism of flow instability responsible for wake oscillations and eddy shedding is approximated well by the

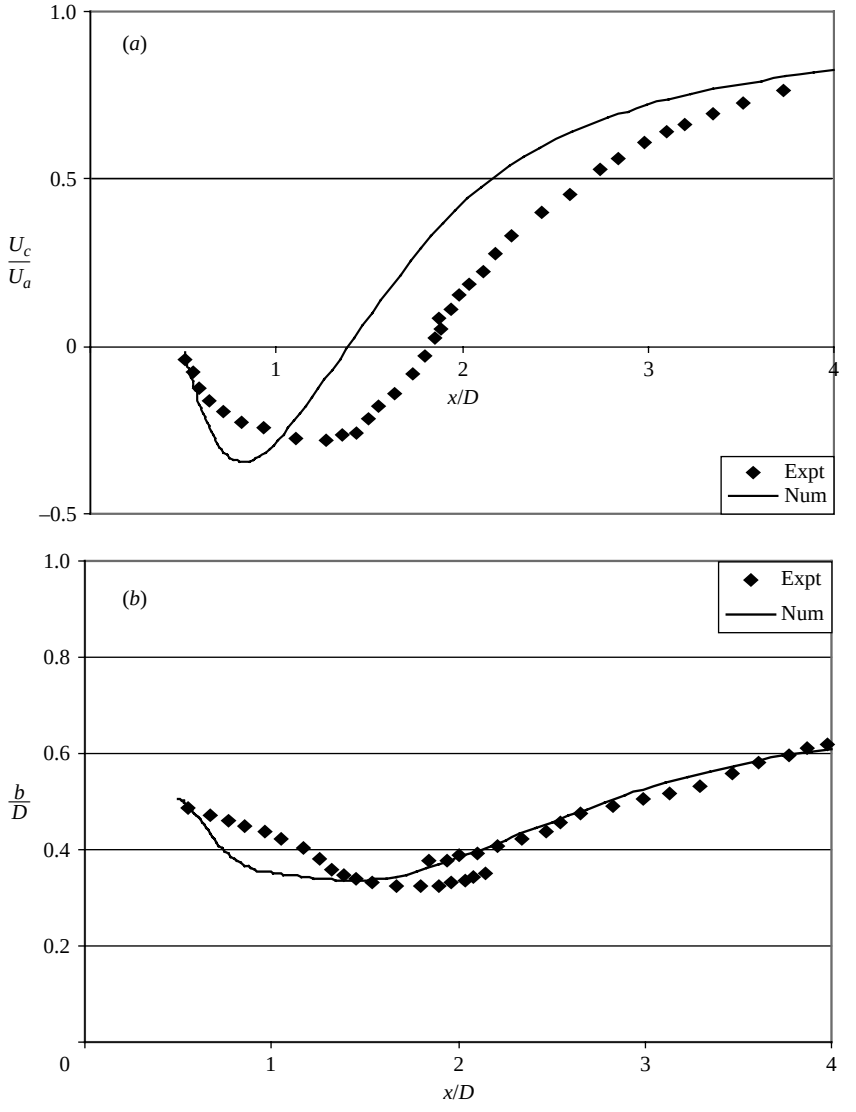

FIGURE 5. Longitudinal development of wake for $S = 0.39$: (*a*) centreline velocity, (*b*) half-width.

nonlinear shallow water model. In addition, the fact that the shallow water model provides a reasonable estimate for the shedding frequency of eddies from the lee of the island is important since the time of trapping of contaminants and/or sediments by the eddies in the wake of an island is a critical parameter for water quality applications.

For a more detailed investigation of the model, the computed mean centreline velocity and wake half-width are compared to the unsteady bubble data in Socolofsky *et al.* (2003). The computed and measured data are shown in figure 5. The magnitude of the maximum return velocity and bubble half-width are in good agreement with the data, but the computed distance from the island to the point of maximum return velocity and the distance from the island to the point of zero return velocity (bubble length) are 30 % shorter than the measured ones. The values of the return velocity and wake

Experiment	U (cm s^{-1})	H (cm)	D (cm)	Re_D	c_f	S	Flow type observed
CY14	6.7	6.0	140	94000	0.0068	0.16	VS
CY43	14.3	2.1	140	200000	0.0074	0.49	UB
CY57	6.9	1.7	140	97000	0.0096	0.79	SB

TABLE 2. Flow conditions for the three test cases.

half-width are important parameters in the quasi-parallel linear stability analysis performed by Chen & Jirka (1997) and others. Therefore, the agreement between model and data in terms of the magnitudes of return velocity and wake half-width means that linear analysis in which the base flow profiles derived from the depth-averaged models are useful for explaining the transition from one wake regime to another. However, these analyses may not produce the correct position of the instability.

The time series and corresponding spectra calculated for $S = 0.79$, $S = 0.49$ and $S = 0.16$ at different spatial locations for the longitudinal and transverse velocity components are now analysed. The flow conditions for the three tests are given in table 2. The experiments in Chen & Jirka (1995) show that $S = 0.79$, $S = 0.49$ and $S = 0.16$ correspond to SB, UB and VS, respectively. The aim here is to investigate how well the shallow water model reproduces these three regimes.

The temporal velocity history for $S = 0.79$ is shown in figure 6. As can be seen from the figure, the velocity reaches a constant value (after a short-time transient), showing that the flow belongs to the stable SB regime. Further numerical experimentation shows that the transition between SB and UB occurs at bed friction number of about 0.55. The amplitude spectra for $S = 0.49$ are shown in figure 7. The presence of coherent structures in the flow at the island is clearly illustrated by the presence of a narrow band of dominant frequencies around the Strouhal number $St = 0.35$.

The measured and computed bubble length for the SB case are now compared. Ideally, this comparison should be made on the basis of data obtained from velocity measurements. Unfortunately, there are no available velocity-based bubble length data for the SB regime. The data in Chen & Jirka (1995) estimate the bubble length on the basis of dye and not velocity spread. Balachandar *et al.* (2000) reports that concentration spread is 1.5 to 2.5 times larger than the velocity spread in the near wake and 1.3 to 1.6 larger in the far wake. Therefore, the additional spread in the data of Chen & Jirka (1995) needs to be estimated prior to carrying out the data/model comparison. The velocity-based bubble length obtained from the data of Socolofsky *et al.* (2003) for $S = 0.39$ is approximately $1.3D$. On the other hand, the dye-based bubble length obtained from the data of Chen & Jirka (1995) for the same S value is approximately $1.8D$. Therefore, it appears that the dye spread is about 38 % higher than velocity spread. Comparison between the model and data shows that the depth-averaged model produces poor SB lengths even when the difference in spread between the dye and velocity is taken into account. For example, the model underestimates the bubble length by 60 % for the case with $S = 0.62$. This discrepancy between model and data shows the limitation of the depth-averaged shallow water model as S increases beyond the UB regime. The reduced accuracy of the depth-averaged model with S is also reported in Lloyd & Stansby (1997*a*, *b*). Lloyd & Stansby (1997*a*) note '... increase in S resulted in less-accurate [depth-averaged] model simulations ... The velocity field predicted by the depth-averaged model bears little similarity to that observed in the laboratory'.

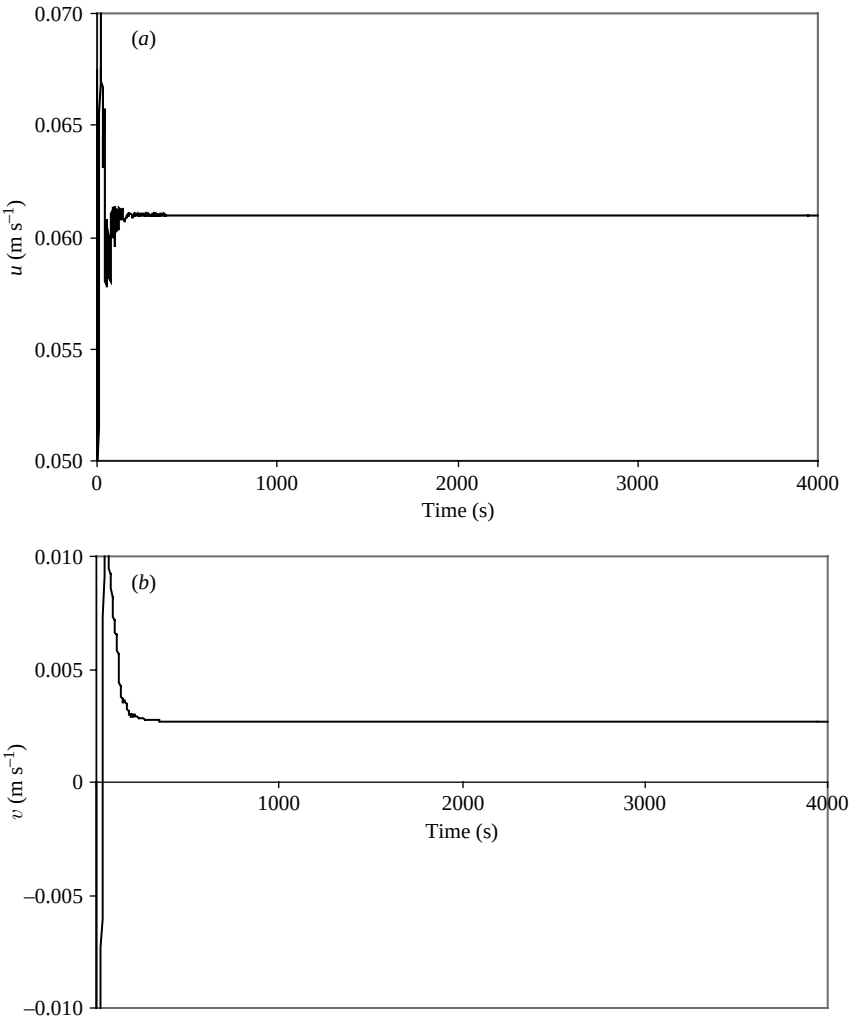

FIGURE 6. The time series of velocity component at locations: $x = 1.2D$, $y = 0.1D$ for $S = 0.79$. (*a*) longitudinal velocity, (*b*) transverse velocity.

The loss of accuracy of the depth-averaged model as S increases is understandable given that the island-generated two-dimensional large-scale turbulence becomes suppressed when S grows, while the bed-generated small-scale three-dimensional turbulence becomes stronger. Indeed, the shallow mixing layer experiments in Uijttewall & Booij (2000) and the grid turbulence experiments in shallow flows in Uijttewall & Jirka (2003) show that increasing S by, say, decreasing the water depth destroys the coherence in the large-scale structures and suppresses the enstrophy cascade mechanism. They found that energy cascade for large S follows closely the $-5/3$ rule, indicative of the three-dimensional nature of the turbulent field. Observed flow features such as the increase in turbulent stresses in the vicinity of bluff bodies, the departure of the vertical profile of velocity from the log-law in the near-wake region, and the strong three-dimensional characteristics of the turbulent field when S increases are not captured by depth-averaged shallow flow models. Recall that depth-averaged models neglect the momentum dispersion associated with the variation of

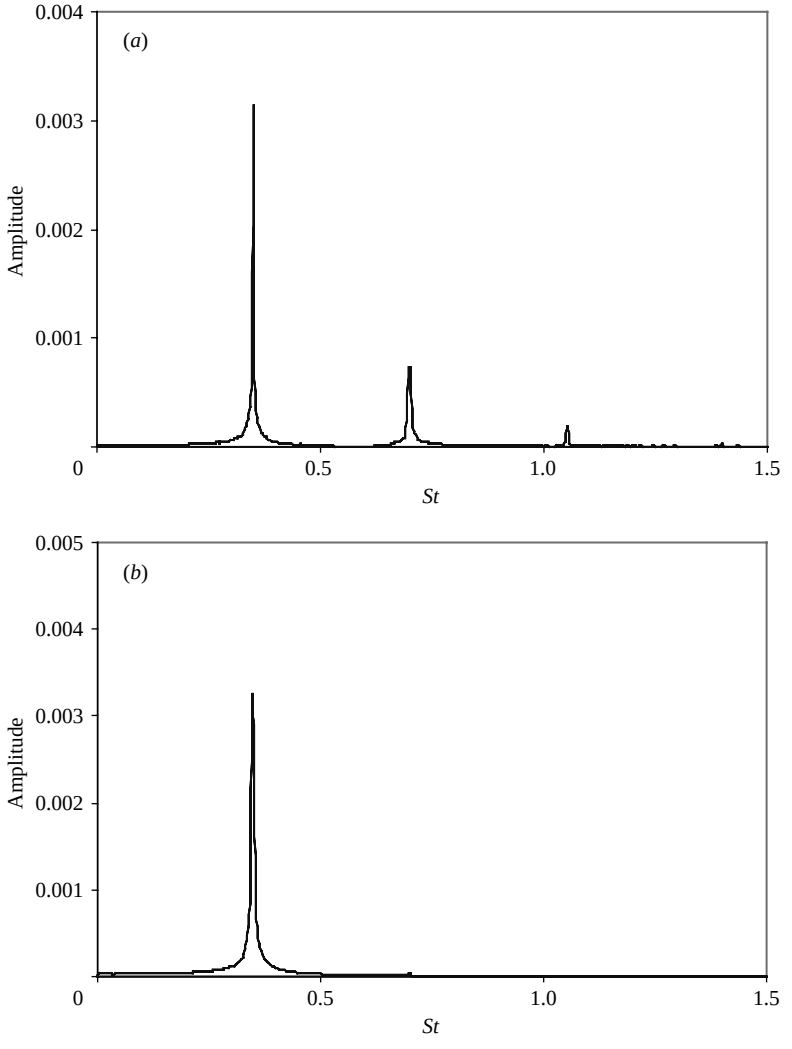

FIGURE 7. Amplitude spectra of longitudinal velocity for $S = 0.49$. (*a*) $x = 1.06D$, $y = 0.02D$; (*b*) $x = 1.73D$, $y = 0.02D$.

velocity with respect to water depth and employ simple quasi-steady wall friction laws to represent bed friction. The three-dimensional results in Stansby (2003) show that the distribution and magnitude of the bottom friction coefficient in the near-wake region is far from constant and becomes large in the vicinity of a bluff body. The value of the friction coefficient in the near-wake region can be much larger than the quasi-steady values used in shallow flow models. In addition, laboratory data reported in Balachandar & Tachie (2001) show that (i) the vertical profiles of the streamwise velocity in the near-wake do not follow the log-law and contain inflection points and (ii) the turbulence intensity increases in the near-wake region. It must also be emphasized that depth-averaged models are also expected to fail when S becomes so small in such a way that the flow can no longer be treated as shallow. As S becomes very small, the vortex shedding and bending becomes important again and the VS regime would break down into three-dimensional flow. The transiton from shallow to deep and the value of S at which this transition occurs has not yet been investigated.

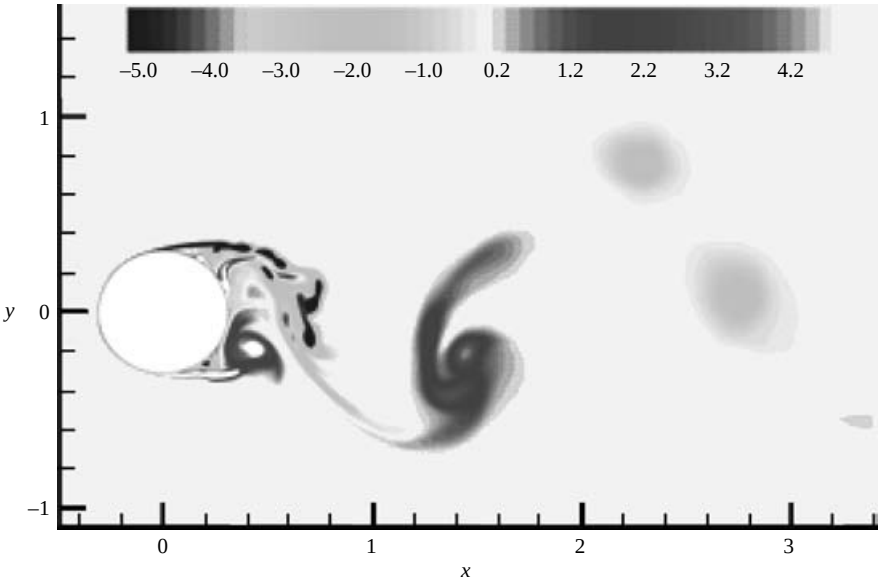

FIGURE 8. The vorticity contours for the case with $S = 0.17$.

The results of this section show that the depth-averaged model becomes unreliable as S increases beyond the S value close to the transition between SB and UB regimes. It is noted that Lloyd & Stansby (1997*a*) found that the depth-averaged shallow model became less accurate than the three-dimensional model when S exceeds 0.3 for the case of conical islands. Similarly, the tests conducted here indicate that the depth-averaged model became inaccurate when S exceeds about 0.55 for the case of cylindrical islands. As a result, the remainder of the paper is restricted to S values in the range [0.17, 0.55].

5. Computed wake patterns

Figures 8–11 show the vorticity contours of shallow wakes in the lee of cylindrical bluff bodies for values of the stability parameter S ranging from 0.17 to 0.51. Figure 8 shows that when $S = 0.17$, the cylinder wake is characterized by a pronounced vortex shedding mechanism, leading to the establishment of a vortex street pattern. The processes of streamline oscillation at the shear layer in the vicinity of the cylinder followed by vortex roll-up and subsequent pairing is clear in these figures. Note that although the Reynolds number is very large ($\approx 10^5$), the shallow wake shown in figure 8 is similar in appearance to the classical von Kármán vortex street found in unbounded plane wakes for small Reynolds number ($\approx 10^2$), highlighting that Reynolds number is not the main control parameter in shallow wake flows. The computed structure of the wake flow in figure 8 is consistent with that observed by Chen & Jirka (1995). The vortices in the wake are highly organized and the flow structure is coherent. The vortex shedding nature of the shallow wake and its associated coherent structure at low values of S is the end product of the absolute instability found by Chen & Jirka (1997).

Further investigation of the unsteady bubble regime is performed for $S = 0.51$ and the near-wake details are plotted in figure 11. It is found that the mean position of the mixing layers at both sides of the cylinder is steady, indicating that the location

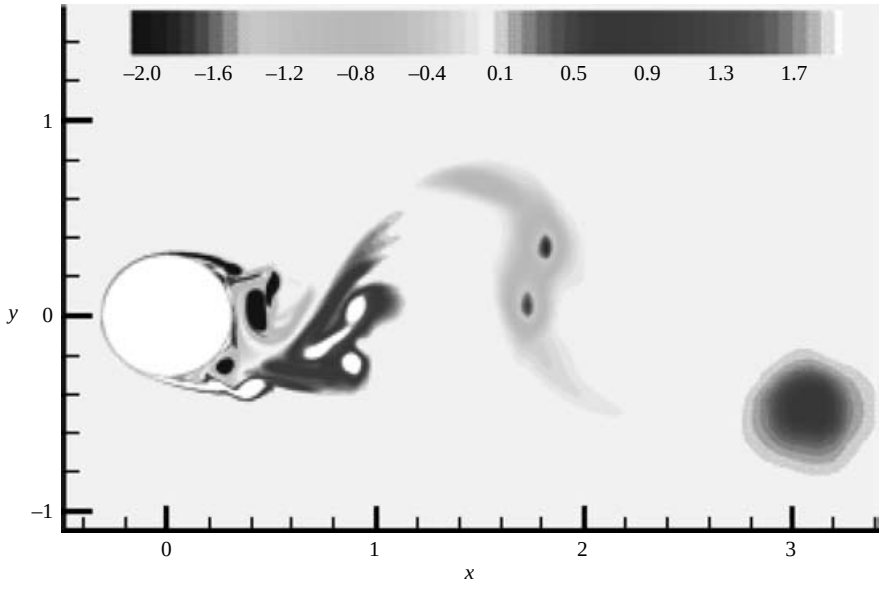

FIGURE 9. The vorticity contours for the case with $S = 0.24$.

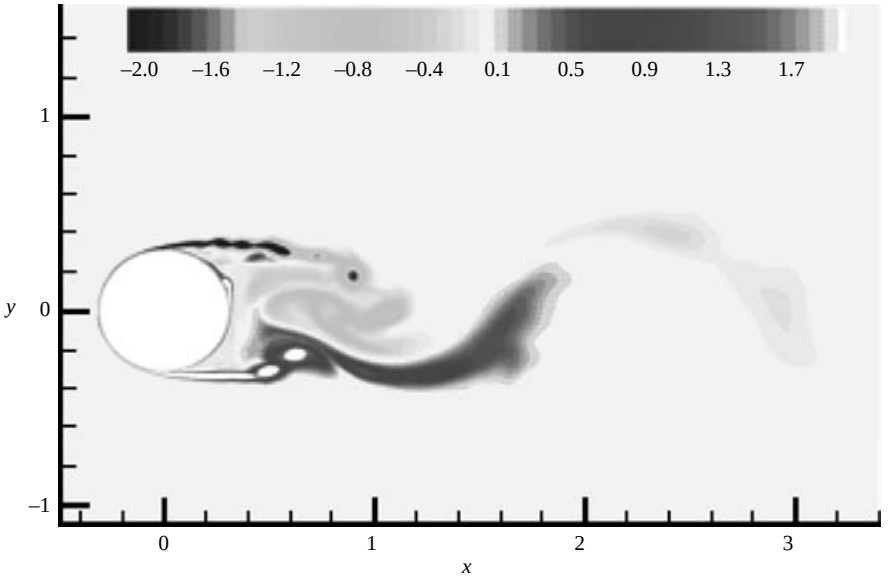

FIGURE 10. The vorticity contours for the case with $S = 0.35$.

of the boundary layer separation point on each side of the bluff body is fixed. Coherent structures exist within these mixing layers as can be seen from fine grid results (figure 11). The two mixing layers converge towards the centreline and merge with one another about 2 island diameters downstream of the aft of the cylinder. The unsteady vortex at the point where the two mixing layers merge triggers a convective-type instability and leads to a wake flapping similar to that found in figure 9 and figure 10. The backflow (reverse flow) within the attached bubble can also be seen clearly in figure 11.

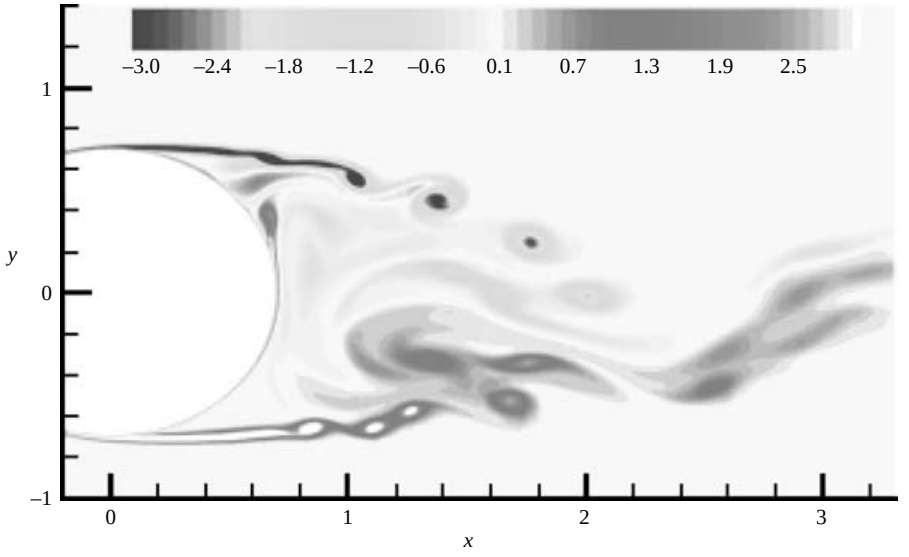

FIGURE 11. Near-wake details for the case with $S = 0.51$.

Figures 9 and 10 show the cylinder wake for $S = 0.24$ and 0.35. An unsteady bubble, characterized by a re-circulating flow region, emerges in the near wake of the cylinder. Downstream of the unsteady bubbles, a sinuous wake is observed. Although not shown here, a time sequence of the sinuous wake reveals that the far wake flaps continuously with respect to the island centreline. The flapping sinuous wake is likely to be the result of the convective instability described in Chen & Jirka (1997). The amplitude of the oscillation of the bubbles and the sinuous wake decreases as S increased from 0.24 to 0.35. The computed structure of the wake flow in figures 8–10 is consistent with that observed by Chen & Jirka (1995). However, the amplitude of the sinuous wake, especially for $S = 0.24$, is more pronounced than that in Chen & Jirka (1995).

6. Absolute instability and the frequency selection criteria

There is ample evidence connecting the global VS frequency and the curve of local absolute instability as function of the streamwise distance for the case of deep flows (e.g. see Pier 2002 and the references given in it). In the context of shallow wakes, Chen & Jirka (1997) used the concepts of convective and absolute instabilities to classify different flow patterns observed in the experiments. The flow is said to be convectively unstable if a perturbation at any fixed location in the laboratory frame decays with time because the localized perturbation travels away and eventually leaves the flow region. The flow is said to be absolutely unstable if perturbations grow in time at any fixed location in the laboratory frame. Chen & Jirka (1997) argued that the transition from steady bubble to unsteady bubble represents the transition from stable to convectively unstable wake. Similarly, the transition from unsteady bubble to vortex street corresponds to the transition from convectively unstable wake to absolutely unstable wake. Schär & Smith (1993) compared the global VS shedding frequency in shallow wakes for the case of zero bottom friction (i.e. $S = 0$) to the frequency obtained from the saddle point criterion as well as the frequency obtained

from the maximum growth criterion. The frequencies obtained from the two selection criteria differ from the shedding frequency by about 30 %.

This section investigates the relation between the local absolute instability and the global VS frequency for the case of shallow wakes. Several criteria for deep wakes are proposed in the literature in an attempt to link the global frequency of oscillations with local absolute stability characteristics (Hannemann & Oertel Jr. 1989; Hammond & Redekopp 1997; Huerre 2000). The criteria in Koch (1985) as well as that in Pier & Huerre (2001) and Pier (2002) are used in this study.

6.1. *Linear model*

Ideally, base flows for linear analysis should be derived from the governing equation. This is not possible for shallow wake flows because an analytical solution for the shallow water equations around a cylinder is not available. Previous stability studies of shallow flows (Chen & Jirka 1997; Kolyshkin & Ghidaoui 2003; Socolofsky *et al.* 2003) use the profile used by Monkewitz (1988) for the analysis of deep-wake flows behind circular cylinders for small Reynolds numbers (up to $Re = 48.5$). It is important to note that although the Monkewitz profile has the salient features of shallow wakes, this profile does not satisfy the shallow water equations.

Here, the base state is obtained by time-averaging of the data obtained from the nonlinear model. The averaging process is given by (4.1). Two base flows considered are obtained from VS and UB data. A typical base flow profile is given in figure 3. The computed profiles differ from that in Monkewitz (1988) by the existence of additional inflection points and by a local flow acceleration in the region between the shear layer and the ambient velocity. These features are also found in the experiments of Socolofsky *et al.* (2003) (see figure 3). The additional inflection points and the flow acceleration at either side of the cylinder are due to the boundary layer that forms at the cylinder wall due to the enforcement of the no-slip condition at the perimeter of the cylinder.

A widely used assumption in the linear stability analysis of shallow shear flows is the rigid-lid assumption. This assumption consists of replacing the gravity-driven free-surface flow by an equivalent pressure-driven flow between two parallel horizontal plates with the top plate being inviscid (acting like a lid) and the bottom plate having the same c_f as the original channel. Field data show that for typical shallow turbulent wakes behind islands the corresponding Froude number of the flow based on the ambient velocity and water depth is about 0.1–0.2 while in the experiments of Chen & Jirka (1995) the Froude number is in the range 0.04 to 0.71. Dimensional analysis shows that the mass storage term in (2.7) (i.e. $\partial \bar{h}/\partial t$) is of order WL_X/UL_Z, while the other terms are of order one. Since the time scale is L_X/U, we obtain $WL_X/UL_Z = A_0/L_Z$, where A_0 is the scale of the wave amplitude. The analysis of Ponce & Simons (1977) and Singh (1996) shows that the amplitude A_0 tends to zero as the Froude number Fr_H (based on water depth) tends to zero. Some estimates of the influence of the Froude number on the stability boundary of transverse shear flows in shallow water flows are presented in Falqués & Iranzo (1994), Ghidaoui & Kolyshkin (1999) and Kolyshkin & Ghidaoui (2002). Falqués & Iranzo (1994) investigated the stability of mean alongshore current in nearshore flows. They found that the error in the growth rates of disturbances due to the rigid-lid assumption (i.e. neglecting $(A_0/L_Z)(\partial h/\partial t)$) for plane sloping beaches is 12 % when the Froude number is 0.63 and 28 % when the Froude number is 0.89. Ghidaoui & Kolyshkin (1999) and Kolyshkin & Ghidaoui (2002) studied the linear stability of transverse shear flows in compound and composite open channels and found that the rigid-lid

assumption works well for weak shear flows and/or small Froude numbers. Thus in general, one can use the rigid-lid assumption within 10 % error in the region $0 < Fr_H < 0.7$ for the calculation of the critical values of the stability parameter S and the rigid-lid assumption is adopted in the linear stability analysis of the paper. This assumption is not used in the nonlinear part.

The rigid-lid assumption entails replacing the gravity-driven open channel by a pressure-driven uniform flow between two parallel plates, the vertical distance between which is $\bar{h}$. Therefore, (2.7) and (2.8) become

$$\frac{\partial \bar{\hat{u}}_\alpha}{\partial x_\alpha} = 0, \tag{6.1}$$

$$\frac{\partial \bar{\hat{u}}_\alpha}{\partial t} + \bar{\hat{u}}_\kappa \frac{\partial \bar{\hat{u}}_\alpha}{\partial x_\kappa} = -\frac{\partial \bar{p}}{\partial x_\alpha} - \frac{1}{2\bar{h}} c_f \bar{u}_\alpha \sqrt{\bar{u}_\kappa \bar{u}_\kappa} + \frac{\partial}{\partial x_\kappa}\left((\nu + \nu_{ev}) \frac{\partial \bar{\hat{u}}_\alpha}{\partial x_\kappa}\right), \tag{6.2}$$

where $\bar{p}$ is the pressure that drives the flow such that $\partial \bar{p}/\partial x_\alpha = \rho g \partial(\bar{h} + b)/\partial x_\alpha$ (i.e. the pressure gradient is equivalent to the sum of the hydrostatic pressure and driving force due to the slope of the bed) and ν_{ev} is the eddy viscosity.

For simplicity, the following notation is adopted in the remainder of the paper: $(u, v) = (\bar{\hat{u}}_1/U, \bar{\hat{u}}_2/U)$, where U is the ambient velocity. Let $(u_0(y), 0, p_0(x))$ define the base flow and consider a perturbed solution to equations (6.1) and (6.2) in the form

$$u = u_0(y) + u'(y)\, \mathrm{e}^{-\lambda t_* + \mathrm{i}kx}, \tag{6.3}$$

$$v = v'(y)\, \mathrm{e}^{-\lambda t_* + \mathrm{i}kx}, \tag{6.4}$$

$$p = p_0(x) + p'(y)\, \mathrm{e}^{-\lambda t_* + \mathrm{i}kx}, \tag{6.5}$$

where u', v' and p' are the complex amplitudes of the normal perturbations, $t_* = Ut/L_X$ is the dimensionless time, k is the wavenumber and $\lambda = \lambda_r + \mathrm{i}\lambda_i$ is a complex eigenvalue. Substituting (6.3)–(6.5) into equations (6.1) and (6.2), linearizing the resulting equations in the neighbourhood of the base flow and eliminating the pressure p' we obtain the following modified Orr–Sommerfeld equation for the function $v'(y)$:

$$\frac{1}{Re_T}\left(\frac{\mathrm{d}^4 v'}{\mathrm{d}y^4} - 2k^2 \frac{\mathrm{d}^2 v'}{\mathrm{d}y^2} + k^4 v'\right) + (\mathrm{i}ku_0 + S_b u_0)\frac{\mathrm{d}^2 v'}{\mathrm{d}y^2} + S_b \frac{\mathrm{d}u_0}{\mathrm{d}y}\frac{\mathrm{d}v'}{\mathrm{d}y}$$
$$- v'\left(\mathrm{i}k \frac{\mathrm{d}^2 u_0}{\mathrm{d}y^2} + \mathrm{i}k^3 u_0 + \frac{S_b}{2} k^2 u_0\right) - \lambda\left(\frac{\mathrm{d}^2 v'}{\mathrm{d}y^2} - k^2 v'\right) = 0, \tag{6.6}$$

where $S_b = c_f/h = c_f L_X/H$ and $Re_T = UL_X/\nu_{ev}$ is the local turbulent Reynolds number based on the constant eddy viscosity ν_{ev}. The turbulent viscosity is estimated from the relation (see Fischer *et al.* 1979)

$$\nu_{ev} = 0.15\sqrt{c_f/2}\, UH. \tag{6.7}$$

The values of Re_T are of order $10^3 - 10^4$ for all cases considered. Calculations with different values of Re_T support the conclusion of Chen & Jirka (1997) that the stability characteristics are insensitive to Re_T once $Re_T > 1000$. As mentioned before, the terms proportional to $1/Re_T$ are included for numerical stability: the inviscid version of (6.6) is singular if the region of reverse flow is present since $u_0(y) = 0$ at some points of the flow. The boundary conditions for the function v' are

$$v'(\pm\infty) = 0, \qquad \frac{\mathrm{d}v'}{\mathrm{d}y}(\pm\infty) = 0. \tag{6.8}$$

The problem (6.6)–(6.8) is an eigenvalue problem. The eigenvalues, $\lambda_s = \lambda_{rs} + \mathrm{i}\lambda_{is}$, $s = 1, 2, \ldots$, determine the linear stability of the base flow given by $(u_0(y), 0, p_0(x))$. This base flow is said to be linearly stable if $\lambda_{rs} > 0$ for all s, and linearly unstable if $\lambda_{rs} < 0$ for at least one value of s.

The linear stability problem (6.6)–(6.8) is solved by a pseudospectral collocation method based on Chebyshev polynomials (the details of the numerical method are given in Ghidaoui & Kolyshkin 1999). Essentially, the problem is reduced to the following generalized eigenvalue problem:

$$(\boldsymbol{B} - \lambda \boldsymbol{C})\boldsymbol{\psi} = 0, \tag{6.9}$$

where

$$\boldsymbol{\psi} = [a_1, a_2 \ldots a_m, b_1, b_2 \ldots b_m, c_1, c_2 \ldots c_m]^T.$$

where the superscript T denotes transpose. Equation (6.9) is solved by the IMSL routine GVLCG (IMSL 1991). The current solution is more convenient than those obtained by traditional collocation methods (Canuto *et al.* 1988) for two reasons. First, in the present case the matrix $\boldsymbol{C}$ is not singular. Second, the definition of base functions in terms of the Chebyshev polynomials, which satisfy the given boundary conditions, considerably reduces the condition number of the matrices in this method (Heinrichs 1989).

6.2. *Results and discussion*

The stability analysis of mean velocity profiles obtained from the nonlinear model is performed in this section. It follows from (6.6) that the stability parameter S_b is defined in terms of the wake half-width L_X while the experimental patterns in Chen & Jirka (1995) were classified using the S value (which is defined in terms of D). The relation between the two parameters is $S = S_b D/L_X$. Since the nonlinear model allows one to calculate L_X for each position downstream, the link between the parameter S reported in experiments of Chen & Jirka (1995) and the parameter S_b used in stability calculations can be easily established.

The critical values, S_c, of the parameter S_b are calculated as follows. First, the set of all points in the (k, S)-plane for which one eigenvalue satisfies the condition $\lambda_r = 0$ while all other eigenvalues have positive real parts is obtained (we denote this set by $S_b(k)$). Second, the critical value, S_c, of the stability parameter S_b is defined as the maximum, over all k, of the values $S_b(k)$ of S_b:

$$S_c = \max_k S_b(k). \tag{6.10}$$

In order to determine the boundary between a convectively and an absolutely unstable wake the search for a saddle point is performed in the (k, λ)-domain (Huerre 2000). In this case both k and λ are assumed to be complex of the form $k = k_r + \mathrm{i}k_i$, $\lambda = \lambda_r + \mathrm{i}\lambda_i$. The dividing line between convective and absolute instability is calculated as follows. Assuming $\lambda_r = 0$ we perform an eigenvalue search at a fixed downstream station for different k_r, k_i and S in order to find a saddle point. The procedure is repeated for different downstream stations. The results are presented in figure 12 for the VS and UB cases. The horizontal dashed lines correspond to the experimental values of the parameter S for the two cases.

Basic state–VS: Figure 12 shows that the flow is locally absolutely unstable in the interval $(0 \leqslant x_1/D \leqslant x_{ac} = 0.37)$ for the VS case, where x_{ac} denotes the downstream location at which the instability changes from absolute to convective. This pattern of spatial distribution where the absolute instability occurs at the upstream end of

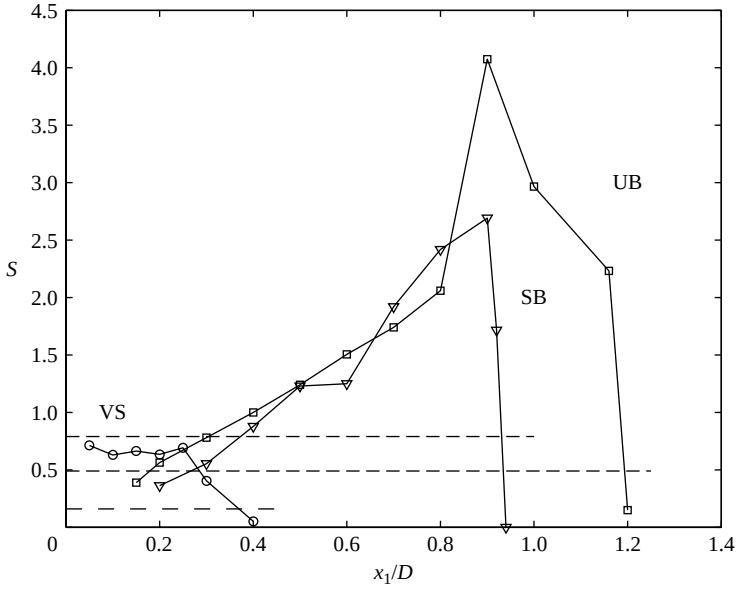

FIGURE 12. The absolute instability boundary versus x_1/D for $S = 0.79$ (triangles), $S = 0.49$ (squares) and $S = 0.16$ (circles).

the flow followed by a convective instability arises in semi-infinite domains (Chomaz 2005). The Koch (1985) criterion where the global frequency is determined by the local absolute frequency at the downstream station x_{ac}, is used in this case. The value of the Strouhal number obtained from the dominant frequency of the VS regime is $St_n = 0.217$. The value of St at x_{ca} obtained from Koch's criterion is 0.208. The good agreement between the frequency obtained from the linear analysis of the basic state obtained from the VS regime and the nonlinear frequency has also been found in Pier (2002), but for the case where St was evaluated at the point of transition from convective to absolute instability (i.e. at x_{ca}). The value of St at x_{ca} cannot be obtained here since the flow appears to be absolutely unstable next to the cylinder for the VS case.

The good agreement between the St obtained from Koch's criterion and the St obtained from the nonlinear code is probably due to the fact that the basic state is determined from a time average of the VS data. That is, the instability of a basic state obtained by averaging in time VS data does not describe a transition to another regime; instead, it shows that the non-oscillatory time-mean basic state for $S = 0.16$ is not observable and the flow reverts back to the VS street from which the basic state is derived. Therefore, the close agreement indicates that the stability analysis of mean base flows obtained by averaging the VS data is able to rediscover the dynamics of the very flow that the basic state is obtained from. However, this approach cannot explain the mechanism responsible for the establishment of the VS regime. It may be tempting to argue that the good agreement between the shedding frequency obtained from the linear and nonlinear analysis may at least be used to save computational time if one estimates the shedding frequency by a linear model in lieu of a nonlinear model. Unfortunately, we find that the computational time and effort required to solve the linear model and determine the absolute instability curve is comparable to that for solving the nonlinear model.

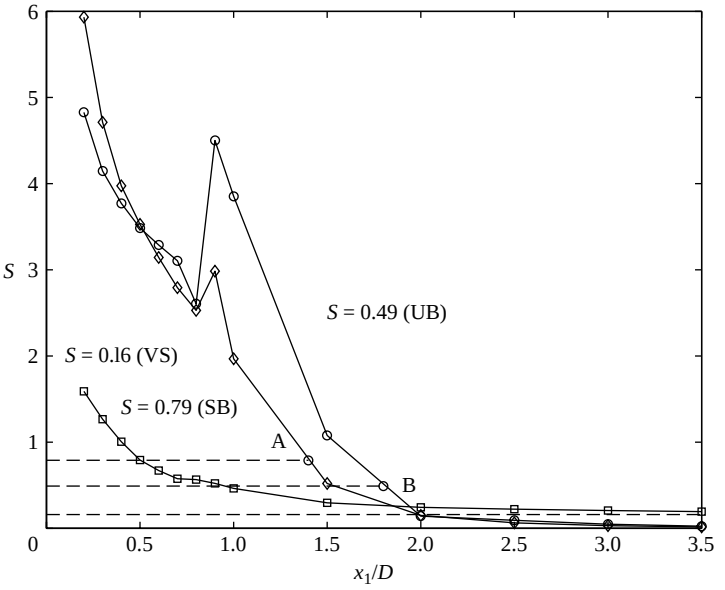

FIGURE 13. The advective instability boundary versus x_1/D for $S = 0.79$ (diamonds), $S = 0.49$ (circles) and $S = 0.16$ (squares).

Basic State–UB but near the transition to VS: The above results show that one cannot expect to understand the onset of a VS regime by perturbing a state derived from the VS regime itself. Its understanding requires the perturbation of a basic state that has the properties of the UB regime. The case studied is for $S = 0.49$ (about 20 % below the value that defines the transition from UB to VS). Figure 12 shows that the basic state for $S = 0.49$ is locally absolutely unstable in the region $0.18 < x_1/D < 1.19$. Here, x_{ca} denotes the upstream point where the transition from convective to absolute instability occurs. The results show that the mean base flow obtained from the UB data is convectively unstable in the region $0 \leqslant x_1/D \leqslant x_{ca}$, absolutely unstable in the region $x_{ca} \leqslant x_1/D \leqslant x_{ac}$, convectively unstable in the region $x_{ac} \leqslant x_1/D \leqslant x_{cs}$, and stable in the region $x_1/D \geqslant x_{cs}$. The coordinate x_{cs} is the location beyond which the flow becomes stable. The values of x_{cs} for $S = 0.79$ and $S = 0.49$ are found to be 1.4 and 1.8, respectively (see figure 13). It is noted that reducing the value of S increases the region of absolute instability and that the two absolute instability curves are close to each other in the region 0.2 to about 0.8.

The aim here is to connect the local absolute instability to the global instability. The linear results, which are based on the local parallel assumption, provide a wide range of absolutely unstable frequencies each of which is associated with a particular spatial position in the absolutely unstable range. Chen & Jirka (1997) found good agreement between the measured global (shedding) frequency and the frequency of the absolutely unstable mode that has the maximum growth rate. Here, we investigate the selection criterion proposed in Koch (1985) and on proposed in Pier & Huerre (2001) and in Pier (2002). Pier & Huerre (2001) and Pier (2002) suggest that the global frequency corresponds to the local absolute frequency at the downstream station x_{ca}. The Strouhal number obtained from Koch's criterion for $S = 0.49$ is $St_{ac} = 0.486$. This value is far from the global Strouhal number of 0.392. On the other hand, the Strouhal number obtained from the criterion in Pier & Huerre (2001) and Pier (2002)

for $S = 0.49$ is $St_{ac} = 0.306$. This value seems to show that St_{ac} converges towards the global frequency as S is reduced towards the transitional value from UB to VS.

The convergence of St_{ac} towards the global shedding frequency as S decreases for the case of shallow flows is similar to the deep-wake results of Pier (2002) where he also found that St_{ac} became progressively closer to the global shedding frequency as Reynolds number is increased from 50 to about 170. This appears to suggest that the 'wave-maker' mechanism proposed by Pier & Huerre (2001) and Pier (2002) to explain the formation of the VS regime for the case of deep flows remains valid for the shallow wake flows. This is perhaps not surprising since the large-scale VS motion for shallow flows has been found to be similar to low Reynolds number VS motion in deep flows (e.g. Wolanski *et al.* 1984; Ingram & Chu 1987; Chen & Jirka 1997; Uijttewaal & Jirka 2003). Essentially, the influence of the small-scale turbulent eddy viscosity on large-scale VS motion in shallow wakes appears to be similar to the influence of molecular viscosity on VS motion for low Reynolds number deep wakes.

Given its potential importance to shallow flows, the 'wave-maker' mechanism proposed by Pier & Huerre (2001) and Pier (2002) is briefly described. Impulses (perturbations) experience amplitude growth as they move downstream in the convectively unstable region $x_1/D \leqslant x_{ca}$. In addition, the amplitude of the envelope of perturbations in the absolutely unstable region $x_{ca} \leqslant x_1/D \leqslant x_{ac}$ grows and advances in the upstream direction. A 'pile-up' of perturbations occurs at the junction of the absolute and convective regions located at x_{ca}. The nonlinear terms become more significant as the amplitude of the perturbations at the junction grows and a saturation state is eventually reached. The perturbations front x_{ca} plays the role of 'wave-maker'. The frequency of oscillation of the 'wave-maker' is governed by the frequency of the local absolute instability at x_{ca}.

7. Amplitude spectra and sensitivity to external forcing

Figure 7 showed that the flow is nearly, but not purely, periodic. In particular, the amplitude spectra are characterized by a narrow band of dominant frequencies, but secondary small-amplitude instabilities are beginning to emerge. The unstable frequency obtained from linear analysis and the global frequency obtained from experimental data agree with the dominant frequency in figure 7.

According to the classification presented by Chen & Jirka (1997) the unsteady bubble case corresponds to transition from a stable to a convectively unstable wake. Convectively unstable flows are known to behave as noise amplifiers (Huerre & Rossi 1998). In particular, Deissler (1987) used a generalized Ginzburg–Landau equation with an additional term representing the first-order derivative with respect to the spatial coordinate to model convectively unstable flows in the presence of microscopic external noise. He showed that a noise-sustained structure is formed as a result of selective amplification of the noise. Thus, the microscopic external noise plays an important role in the macroscopic dynamics of the flow. Taking into account the above results it is plausible to assume that irregularities in the velocity patterns in figure 7 are observed as a result of noise amplification. The noise in this case could be due to numerical errors. This hypothesis has been tested by investigating the sensitivity of the amplitude spectra to a random noise added at the inflow boundary. The amplitude of the velocity noise is set to 20 % of the ambient velocity. The results are given in figure 14 and the energy spetrum is insensitive to the inflow perturbation.

It is clear from the figure that the spectra with and without the random forcing are the same. Therefore, the wide band of small frequencies is not due to noise.

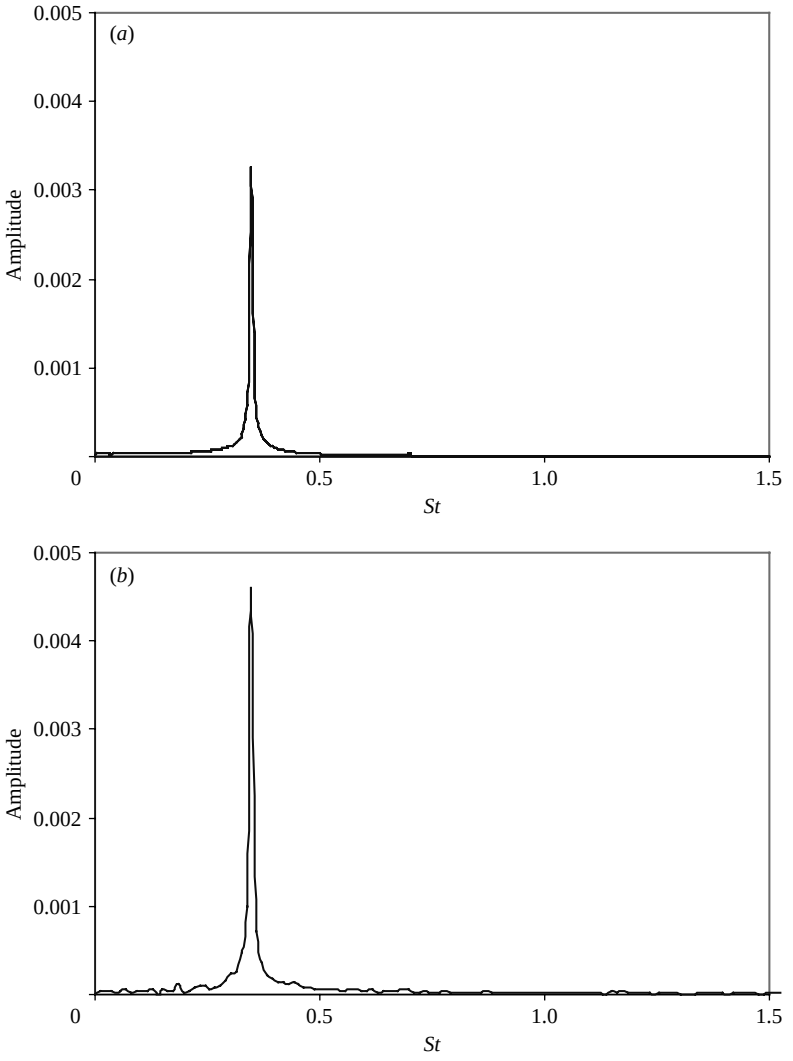

FIGURE 14. Amplitude spectra of longitudinal velocity for $S = 0.49$ at the location $x = 1.73D$, $y = 0.02D$: (*a*) without inflow forcing, (*b*) with inflow forcing.

The spectra are produced for S values well into the UB regime. Therefore, it is plausible that the wide band of small-amplitude frequencies is due to secondary instabilities. This conjecture can be tested using weakly nonlinear analysis. It is shown in Kolyshkin & Ghidaoui (2003) by means of a weakly nonlinear analysis that if the stability parameter S_b is slightly below the critical value (that is, if $S_b = S_c(1-\varepsilon^2)$) then the evolution of the most unstable mode (in the convectively unstable regime) in the reference frame moving with group velocity c_g is described by a nonlinear Ginzburg–Landau equation of the form

$$A_\tau = \sigma A + \delta A_{\xi\xi} - \mu |A|^2 A, \tag{7.1}$$

where A is a slow varying amplitude of the perturbation, $\tau = \varepsilon^2 t$ and $\xi = \varepsilon(x - c_g t)$ are 'slow' time and spatial coordinates, and $\sigma = \sigma_r + \mathrm{i}\sigma_i$, $\delta = \delta_r + \mathrm{i}\delta_i$ and $\mu = \mu_r + \mathrm{i}\mu_i$ are complex coefficients. Explicit formulas for calculation of the coefficients σ, δ and

R	c_1	c_2
−0.2	−0.812	2.157
−0.4	−0.803	2.233
−0.5	−0.800	2.190
−0.6	−0.799	2.096
−0.8	−0.795	1.784
−0.9	−0.798	1.541

TABLE 3. Values of c_1 and c_2 in equation (7.4) for various R values and $N = 1$.

μ are given in Kolyshkin & Ghiadoui (2003). Using the substitutions

$$\tau' = \tau\sigma_r, \quad \xi' = \xi\sqrt{\frac{\sigma_r}{\delta_r}}, \quad A' = A\sqrt{\frac{\mu_r}{\sigma_r}}\,\mathrm{e}^{-\mathrm{i}c_0\sigma_r\tau}$$

equation (7.1) is transformed to the form

$$A'_{\tau'} = A' + (1 + \mathrm{i}c_1)A'_{\xi'\xi'} - (1 + \mathrm{i}c_2)|A'|^2A', \tag{7.2}$$

where

$$c_0 = \frac{\sigma_i}{\sigma_r}, \quad c_1 = \frac{\delta_i}{\delta_r}, \quad c_2 = \frac{\mu_i}{\mu_r}.$$

The Ginzburg–Landau equation is widely used as a model equation in science and engineering. An excellent recent survey of the properties and solutions of equation (7.2) is given by Aronson & Kramer (2002). In particular, it is well-known that equation (7.2) has a plane wave solution of the form

$$A = C\,\mathrm{e}^{\mathrm{i}(K\xi' - \Omega\tau')}. \tag{7.3}$$

Secondary instability of the complex Ginzburg–Landau equation is studied in Couairon & Chomaz (1999) where it is shown, in particular, that a sufficient condition for instability of a plane wave solution is (this type of instability is referred to as the Benjamin–Feir instability)

$$1 + c_1c_2 < 0. \tag{7.4}$$

On the other hand, if the expression $1+c_1c_2$ is positive then solution (7.3) may be either stable or unstable for a finite wavenumber K. In order to see which scenario takes place for shallow wakes we have calculated the coefficients of the Ginzburg–Landau equation (7.2) using the following model profile (Monkewitz 1988):

$$u_0(y) = 1 + \frac{2R}{1 - R}[1 + \sinh^{2N}(\alpha y)]^{-1}, \tag{7.5}$$

where $R = (U_c - U)/(U_c + U)$, $\alpha = \sinh^{-1}(1)$, U_c is the centreline velocity, U is the ambient velocity, L_X is the wake half-width defined as the distance from the axis of the wake such that $U(L_X) = U_* = (U_c + U)/2$, and N is a parameter which reflects the shape of the velocity profile, $N \geqslant 1$. The results in table 3 are for $N = 1$ and several values of R.

Some conclusions can be drawn from table 3. The coefficient c_2 is positive for all R. The local value of the bed friction parameter varies with R, which may explain the variation in c_2 with R. This indicates an amplitude saturation at large times. This is in agreement with results shown in figure 7. In addition, for all cases calculated the instability condition (7.4) is satisfied. Thus, pure periodic waves (7.3) are unstable (and therefore are not observable). This conclusion is consistent with the time series

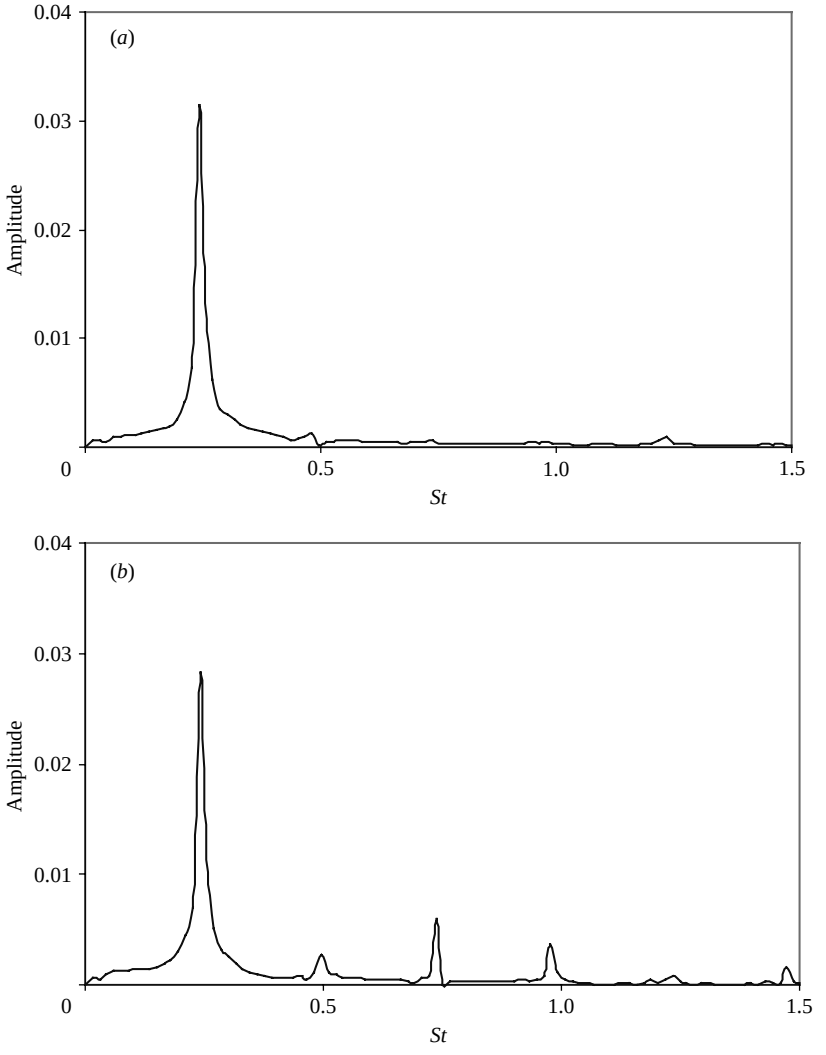

FIGURE 15. Amplitude spectra of longitudinal velocity for $S = 0.16$. (*a*) $x = 1.19D$, $y = 0.02D$; (*b*) $x = 0.73D$, $y = 0.18D$.

data in figure 7, where the observed patterns are clearly not periodic. That is, the wide band of small-amplitude frequencies for the UB case appears to be due to secondary instabilities and not noise.

Figure 15 shows the spectra for the longitudinal velocity components at the two different locations for the vortex street case ($S = 0.16$). The spectrum for the VS case is wider than that of the UB case. The amplitude of the secondary instabilities is also larger than the UB case. The Strouhal number corresponding to the dominant frequency is about 0.24, which is in very good agreement with the experimental data. Again, the results show that the motion is nearly, but not fully periodic. Although the motion is still dominated by the large-amplitude oscillation associated with the shedding frequency, small-amplitude turbulent fluctuations are also present. The amplitude spectra were found to be insensitive to random forcing at the upstream boundary condition (see figure 16), implying that the wide band of small-amplitude

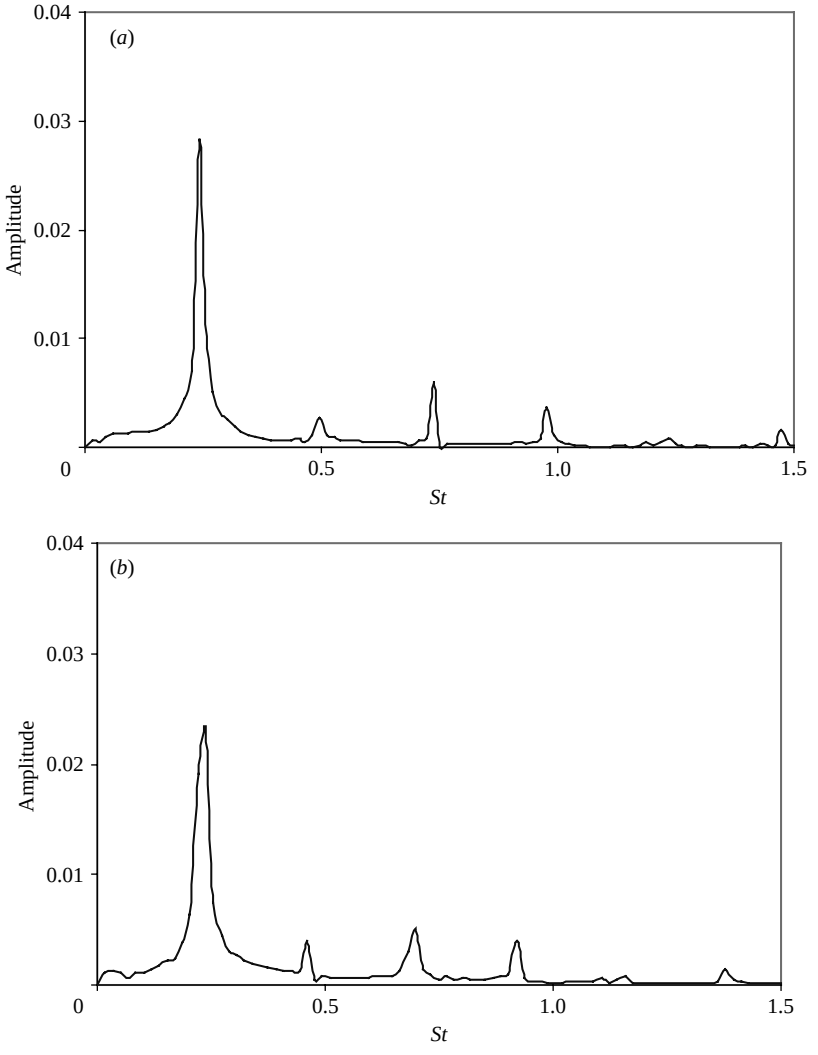

FIGURE 16. Amplitude spectra of longitudinal velocity for $S = 0.16$ at the location $x = 0.73D$, $y = 0.18D$: (*a*) without inflow forcing, (*b*) with inflow forcing.

frequency is not due to noise. The data in figure 16 are produced by prescribing a broad-band forcing at the upstream end. The amplitude of the perturbations is equal to 20 % of the inflow velocity. The insensitivity of the VS regime to random noise is consistent with the fact that this regime is governed by absolute instabilities. Absolute instabilities grow locally with time and overwhelm any noise signal. Therefore, the wide band of small-amplitude frequencies as well as the widening of the dominant frequency band are probably due to secondary instabilities. The sensitivity of the VS regime to random perturbation is investigated here. No major differences appear in the spectrum regarding dominant frequency and amplitude.

8. Conclusions

Shallow wake flows behind circular cylinders are investigated using linear, weakly nonlinear and nonlinear analysis. The analysis is based on the classical depth-averaged

shallow water equations in which the bottom friction is represented using the quadratic wall shear law. The nonlinear model is used to compute velocity profiles, shedding frequencies, wake size and wake centreline velocity. Comparison of the computed and measured quantities shows that the depth-averaged shallow water model gives reasonable results for the UB and VS cases, but not for the SB case. The fact that the depth-averaged model becomes less viable for shallow wakes as S increases has also been reported in Lloyd & Stansby (1997*a*, *b*). When S is small, the wake is characterized by large-scale two-dimensional turbulent coherent structures. The influence of the bottom friction and its associated three-dimensional turbulence on these two-dimensional turbulent structures is small when S small. Therefore, flows with small S values such as VS and UB are more amenable to two-dimensional depth-averaged modelling. On the other hand, as S increases, the large-scale two-dimensional turbulent coherent structures become suppressed and begin to lose their coherence due to the increased influence of the bottom friction and its associated three-dimensional turbulence. The numerical tests indicate that the applicability of the depth-averaged model is limited to S values of the order of 0.6 or below. As a result, the stability analyses conducted in this paper are limited to S values below 0.55.

Flow patterns for different values S ranging from 0.17 to 0.51 obtained from the nonlinear numerical simulation are consistent with the flow patterns observed in Chen & Jirka (1995). The processes involved in the formation of large-scale coherent structures in the lee of the island are captured well by the nonlinear model. In particular, a short distance downstream of the cylinder, the shear layer that develops at either side of the cylinder begins to oscillate in the cross-stream direction. The combination of shear layer oscillation and lateral velocity variation cause the streamlines to fold and results in the formation of vortices. These vortices are found to undergo pairing. The dynamics of vortex generation and vortex pairing is governed by the stability parameter S.

A link between the shedding frequency of the fully developed VS and the characteristics of the absolute instability is sought through the selection criteria presented in Koch (1985) and in Pier & Huerre (2001) and Pier (2002). Streamwise time-averaged velocity profiles are computed and used as base flow profiles for the linear analysis. Linear analysis of the time-averaged velocity profile obtained from the VS data gives a region of absolute instability in the vicinity of the cylinder, followed by a region of convective instability, which is in turn followed by a stable region. The frequency obtained from Koch's criterion is in good agreement with the shedding frequency of the VS. Such good agreement is probably due to the fact that the mean base flow is derived from the VS data. That is, linear analysis of a base flow based on the VS data rediscovers the frequency of the very regime that the basic state is obtained from, but cannot reveal the mechanism which governs the shedding frequency. This conclusion is particularly relevant to studies that investigate the stability of experimentally derived time-averaged VS profiles (e.g. Socolofsky *et al.* 2003).

Linear analysis of velocity profiles in the UB regime shows results in an absolutely unstable region sandwiched between two convectively unstable regions. The values of the Strouhal numbers obtained on the basis of the Koch criterion are in poor agreement with the Strouhal number of the fully developed VS. On the other hand, the values of the Strouhal numbers obtained from the criterion given in Pier & Huerre (2001) become closer to the Strouhal number of the fully developed VS. Therefore, the 'wave-maker' mechanism proposed by Pier & Huerre (2001) and Pier (2002) to

explain the formation of the VS regime for the case of deep flows appears to remain valid for shallow wake flows. Essentially, perturbations are expected to pile up at the point of transition from the convectively unstable region to the absolutely unstable region (x_{ca}). This pile-up of perturbations drives the VS motion and the driving frequency governed by the frequency obtained from the local linear analysis at x_{ca}.

The computed velocity spectra for the unsteady bubble regime involve small-amplitude frequencies, associated with secondary instabilities, and a narrow band of dominant frequencies, associated with the primary instability. The computed dominant frequency is in good agreement with the measured frequency. Amplitude velocity spectra are found to be insensitive to random forcing at the inflow boundary, implying that the wide band of small-amplitude frequencies is not due to noise. The values of the coefficients of the Ginzburg–Landau equation are found to belong to the unstable Benjamin–Feir regime, which indicates that the wide band of small-amplitude frequency is due to secondary instabilities that develop when the value of the stability parameter is well into the UB regime. The spectra for the VS case are similar in shape to those of the UB case. However, the amplitude of VS oscillation is larger than that UB while the shedding frequency of the VS is smaller than that of the UB. The computed Strouhal number based on the dominant frequency is around 0.24. The measured VS shedding frequency is about 0.21.

We are indebted to the anonymous reviewers for their highly constructive comments. This work is supported by the Research Grants Council of Hong Kong under Project No. HKUST6092/00E.

Appendix

The explicit form of the net flux is

$$\boldsymbol{F}+\boldsymbol{F}_{t_c}=\alpha_1\{\boldsymbol{a}_-+\boldsymbol{a}_+\}+\alpha_2\{\boldsymbol{n}\cdot\nabla(\boldsymbol{b}_-+\boldsymbol{b}_+)+\boldsymbol{t}\cdot\nabla(\boldsymbol{d}_-+\boldsymbol{d}_+)\}+\left(\alpha_3+\alpha_5\frac{\partial}{\partial t}\right)\boldsymbol{e}$$
$$+\alpha_4\{\boldsymbol{n}\cdot\nabla\boldsymbol{g}+\boldsymbol{t}\cdot\nabla\boldsymbol{k}\} \tag{A 1}$$

where $V_n=\hat{\bar{u}}_n/\sqrt{g\bar{h}}$; $\alpha_1(t)=\exp(-(t-t^k)/t_c)$; $\alpha_2(t)=-(t-t^k)\alpha_1(t)$; $\alpha_3(t)=1-\alpha_1$; $\alpha_4(t)=t_c(-1+\alpha_1(t))+(t-t^k)\alpha_1(t)$; and $\alpha_5(t)=(t-t^k)+t_c(-1+\alpha_1(t))$. The vectors $\boldsymbol{a}_-$, $\boldsymbol{b}_-$ and $\boldsymbol{d}_-$ are evaluated at x_α^-; $\boldsymbol{a}_+$, $\boldsymbol{b}_+$ and $\boldsymbol{d}_+$ are evaluated at x_α^+ and $\boldsymbol{e}$, $\boldsymbol{g}$ and $\boldsymbol{k}$ are evaluated at x_α (i.e. on $\partial\Omega_{ij}$). The explicit forms of these vectors are

$$\boldsymbol{a}_-=\frac{\bar{h}_-\sqrt{g\bar{h}_-}}{2}\begin{bmatrix}V_n\mathrm{erfc}(-V_n)+(1/\sqrt{\pi})\mathrm{e}^{-V_n^2}\\ \left(V_n\hat{\bar{\boldsymbol{u}}}+\boldsymbol{n}\tfrac{1}{2}\sqrt{g\bar{h}}\right)\mathrm{erfc}(-V_n)+\hat{\bar{\boldsymbol{u}}}\mathrm{e}^{-V_n^2}/\sqrt{\pi}\end{bmatrix}_-, \tag{A 2}$$

$$\boldsymbol{a}_+=\frac{\bar{h}_+\sqrt{g\bar{h}_+}}{2}\begin{bmatrix}V_n\mathrm{erfc}(V_n)-(1/\sqrt{\pi})\mathrm{e}^{-V_n^2}\\ \left(V_n\hat{\bar{\boldsymbol{u}}}+\boldsymbol{n}\tfrac{1}{2}\sqrt{g\bar{h}}\right)\mathrm{erfc}(V_n)-\hat{\bar{\boldsymbol{u}}}\mathrm{e}^{-V_n^2}/\sqrt{\pi}\end{bmatrix}_+, \tag{A 3}$$

$$\boldsymbol{b}_-=\frac{g\bar{h}_-^2}{2}\begin{bmatrix}\left(V_n^2+\tfrac{1}{2}\right)\mathrm{erfc}(-V_n)+V_n\mathrm{e}^{-V_n^2}/\sqrt{\pi}\\ \left(V_n^2\hat{\bar{\boldsymbol{u}}}+\tfrac{1}{2}\hat{\bar{\boldsymbol{u}}}+\hat{\bar{u}}_n\boldsymbol{n}\right)\mathrm{erfc}(-V_n)+\left(V_n\hat{\bar{\boldsymbol{u}}}+\sqrt{g\bar{h}}\boldsymbol{n}\right)\mathrm{e}^{-V_n^2}/\sqrt{\pi}\end{bmatrix}_-, \tag{A 4}$$

$$\boldsymbol{b}_+=\frac{g\bar{h}_+^2}{2}\begin{bmatrix}\left(V_n^2+\tfrac{1}{2}\right)\mathrm{erfc}(V_n)-V_n\mathrm{e}^{-V_n^2}/\sqrt{\pi}\\ \left(V_n^2\hat{\bar{\boldsymbol{u}}}+\tfrac{1}{2}\hat{\bar{\boldsymbol{u}}}+\hat{\bar{u}}_n\boldsymbol{n}\right)\mathrm{erfc}(V_n)-\left(V_n\hat{\bar{\boldsymbol{u}}}+\sqrt{g\bar{h}}\boldsymbol{n}\right)\mathrm{e}^{-V_n^2}/\sqrt{\pi}\end{bmatrix}_-, \tag{A 5}$$

$$\boldsymbol{d}_- = \frac{\bar{h}_-\sqrt{g\bar{h}_-}}{2}\begin{bmatrix} \hat{\bar{u}}_t\{V_n\mathrm{erfc}(-V_n) + \mathrm{e}^{-V_n^2}/\sqrt{\pi}\} \\ \hat{\bar{u}}_t\sqrt{g\bar{h}}\{(V_n^2+\tfrac{1}{2})\mathrm{erfc}(-V_n) + 3V_n\mathrm{e}^{-V_n^2}/\sqrt{\pi}\} \\ \{\hat{\bar{u}}_t^2 + \tfrac{1}{2}g\bar{h}\}\{V_n\mathrm{erfc}(-V_n) + \mathrm{e}^{-V_n^2}/\sqrt{\pi}\} \end{bmatrix}_-, \tag{A 6}$$

$$\boldsymbol{d}_+ = \frac{\bar{h}_+\sqrt{g\bar{h}_+}}{2}\begin{bmatrix} \hat{\bar{u}}_t\{V_n\mathrm{erfc}(V_n) - \mathrm{e}^{-V_n^2}/\sqrt{\pi}\} \\ \hat{\bar{u}}_t\sqrt{g\bar{h}}\{(V_n^2+\tfrac{1}{2})\mathrm{erfc}(V_n) - 3V_n e^{-V_n^2}/\sqrt{\pi}\} \\ \{\hat{\bar{u}}_t^2 + \tfrac{1}{2}g\bar{h}\}\{V_n\mathrm{erfc}(V_n) - \mathrm{e}^{-V_n^2}/\sqrt{\pi}\} \end{bmatrix}_+, \tag{A 7}$$

$$\boldsymbol{e} = h\begin{bmatrix} \hat{\bar{u}}_n \\ \hat{\bar{u}}_n\hat{\bar{\boldsymbol{u}}} + \tfrac{1}{2}g\bar{h}\boldsymbol{n} \end{bmatrix}, \tag{A 8}$$

$$\boldsymbol{g} = \bar{h}\begin{bmatrix} \hat{\bar{u}}_n^2 + \tfrac{1}{2}gh \\ \hat{\bar{u}}_n^2\hat{\bar{\boldsymbol{u}}} + \tfrac{3}{2}g\bar{h}\hat{\bar{u}}_n\boldsymbol{n} \end{bmatrix}_s, \tag{A 9}$$

$$\boldsymbol{k} = \bar{h}\begin{bmatrix} \hat{\bar{u}}_n\hat{\bar{u}}_t \\ \hat{\bar{u}}_n\hat{\bar{u}}_t\hat{\bar{\boldsymbol{u}}} + (\hat{\bar{u}}_t\boldsymbol{n} + \hat{\bar{u}}_n\boldsymbol{t})\tfrac{1}{2}g\bar{h} \end{bmatrix}. \tag{A 10}$$

Relations (A 1) through (A 10) provide the BGK-based algorithm for the net flux from (i, j). The flow depth and velocities and their slopes at x_α^+, x_α are x_α^- are evaluated using the standard Monotonic Upstream-centred Scheme for Conservation Laws (MUSCL) limiter.

REFERENCES

Balachandran, R., Ramachandran, S. & Tachie, M. F. 2000 Characteristics of shallow turbulent near wakes at low Reynolds numbers. *Trans. ASME*: *J. Fluids Engng* **122**, 302–308.

Balachandran, R. & Tachie, M. F. 2001 A study of boundary layer-wake interaction in shallow open channel flows. *Exps. Fluids* **30**, 511–521.

Balachandran, R., Tachie, M. F. & Chu, V. H. 1999 Concentration profiles in shallow turbulent wakes. *Trans. ASME*: *J. Fluids Engng* **121**, 34–43.

Canuto, C., Hussaini, M. Y., Quarteroni, A. & Zang, T. A. 1988 *Spectral Methods in Fluid Dynamics*. Springer.

Chen, D. & Jirka, G. H. 1995 Experimental study of plane turbulent wake in a shallow water layer. *Fluid Dyn. Res.* **16**, 11–41.

Chen, D. & Jirka, G. H. 1997 Absolute and convective instabilities of plane turbulent wakes in a shallow water layer. *J. Fluid Mech.* **338**, 157–172.

Chen, D. & Jirka, G. H. 1998 Linear stability analysis of turbulent mixing layers and jets in shallow water layers. *J. Hydr. Res.* **36**, 815–830.

Chen, H., Chen, S. & Matthaeus, W. H. 1992 Recovery of the Navier–Stokes equations using a lattice-gas Boltzmann Method. *Phys. Rev.* A **45**, 5339–5342.

Chen, S. & Doolen, G. D. 1998 Lattice Boltzmann method for fluid flows. *Annu. Rev. Fluid Mech.* **30**, 329–364.

Chomaz, J.-M. 2005 Global instabilities in spatially developing flows: Non-normality and nonlinearity. *Annu. Rev. Fluid Mech.* **37**, 357–392.

Chu, V. H. & Babarutsi, S. 1988 Confinement and bed-friction effects in shallow turbulent mixing layers. *J. Hydr. Engng* **114**, 1257–1274.

Chu, V. H., Wu, J. H. & Khayat, R. E. 1983 Stability of turbulent shear flows in shallow channel. *Proc. XX Congress IAHR, Moscow, USSR*, vol. 3, pp. 128–133.

Chu, V. H., Wu, J. H. & Khayat, R. E. 1991 Stability of transverse shear flows in shallow open channels. *J. Hydr. Engng* **117**, 1370–1388.

Couairon, A. & Chomaz, J.-M. 1999 Primary and secondary nonlinear global instability *Physica* D **132**, 428–456.

Deissler, R. J. 1987 Spatially growing waves, intermittency, and convectice chaos in an open-flow system. *Physica* D **25**, 233–260.

Falqués, A. & Iranzo, V. 1994 Numerical simulation of vorticity waves in the nearshore *J. Geophys. Res.* **99**, 825–841.

Fischer, H. B., List, E. J., Koh, R. C. Y., Imberger, J. & Brook, N. 1979 *Mixing in Inland and Coastal Waters*. Academic.

Ghidaoui, M. S., Deng, J. Q., Gray, W. G. & Xu, K. 2001 A Boltzmann based model for open channel flows. *Intl J. Numer. Meth. Fluids* **35**, 449–494.

Ghidaoui, M. S. & Kolyshkin, A. A. 1999 Linear stability analysis of lateral motions in compound open channels. *J. Hydr. Engng* **125**, 871–880.

Grubišić, V., Smith, R. B. & Schär, C. 1995 The effect of bottom friction on shallow-water flow past an isolated obstacle. *J. Atmos. Sci.* **52**, 1985–2005.

Gunstensen, A. K., Rothman, D. H., Zaleski, S. & Zanetti, G. 1991 Lattice Boltzmann model of immiscible fluids. *Phys. Rev.* A **43**, 4320-4327.

Hammond, D. A. & Redekopp, L. G. 1997 Global dynamics of symmetric and asymmetric wakes. *J. Fluid Mech.* **331**, 231–260.

Hannemann, K., & Oertel, H., Jr. 1989 Numerical simulation of the absolutely and convectively unstable wake. *J. Fluid Mech.* **199**, 55–88.

Heinrichs, W. 1989 Improved condition number for spectral methods. *Math. Comput.* **53**, 103–119.

Hinze, J. O. 1987 *Turbulence*, 2nd Edn. McGraw-Hill.

Hinterberger, C., Frohlich, J. & Rodi, W. 2003 Three-dimensional and depth-average large eddy simulation of shallow water flows. In *Proc. Intl Symposium on Shallow Flows, Delft*, vol. 3. pp. 67–74.

Huerre, P. 2000 Open shear flow instabilities. In *Perspectives in Fluid Dynamics* (ed. G. K. Batchelor, H. K. Moffatt & M. G. Worster). Cambridge University Press.

Huerre, P. & Rossi, M. 1998 Hydrodynamic instabilities in open flows. In *Hydrodynamics and Nonlinear Instabilities* (ed. C. Godréche & P. Manneville). Cambridge University Press.

IMSL 1991 Fortran subroutines for mathematical applications. *IMSL MATH/LIBRARY, ver. 2.0.*

Ingram, R. G. & Chu, V. H. 1987 Flow around islands in Rupert Bay: An investigation of the bottom friction effect. *J. Geophys. Res.* **92**, 14521–14533.

Jirka, G. H. 2001 Large scale flow structures and mixing processes in shallow flows. *J. Hydraul. Res.* **39**, 567–573.

Koch, W. 1985 Local instability characteristics and frequency determination of self-excited wake flows. *J. Sound Vib.* **99**, 53–83.

Kolyshkin, A. A. & Ghidaoui, M. S. 2002 Gravitational and shear instabilities in compound and composite channels. *J. Hydr. Engng* **128**, 1076–1086.

Kolyshkin, A. A. & Ghidaoui, M. S. 2003 Stability analysis of shallow wake flows. *J. Fluid Mech.* **494**, 355–377.

Liang, J. H., Ghidaoui, M. S., Deng, J. Q. & Gray, W. G. 2005 A Boltzmann–based finite volume algorithm for surface water flows on cells of arbitary shapes. *J. Hydr. Res.* (In press).

Lloyd, P. M. & Stansby, P. K. 1997*a* Shallow-water flow around model conical islands of small side slope. I: Surface piercing. *J. Hydr. Engng* **123**, 1057–1067.

Lloyd, P. M. & Stansby, P. K. 1997*b* Shallow-water flow around model conical islands of small side slope. II: Submerged. *J. Hydr. Engng* **123**, 1068–1077.

Mellor, G. L. 2004 *User Guide for a Three-dimensional, Primitive Equation, Numerical Ocean Model.* http://www.aos.princeton.edu/WWWPUBLIC/htdocs.pom/

Monkewitz, P. A. 1988 The absolute and convective nature of instability in two-dimensional wakes at low Reynolds numbers. *Phys. Fluids* **31**, 999–1006.

Oey, L.-Y., Ezer, T. & Lee, H.-C. 2005 Loop current, rings and related circulation in the gulf of Mexico: a review of numerical models and future challenges. In *Ocean Circulation in the Gulf of Mexico* (ed. W. Sturges & A. L. Fernandez). AGU Monograph (in press).

Pedlosky, J. 1987 *Geophysical Fluid Dynamics*. Springer.

Pier, B. 2002 On the frequency selection of finite-amplitude vortex shedding in the cylinder wake. *J. Fluid Mech.* **458**, 407–417.

Pier, B. & Huerre, P. 2001 Nonlinear self-sustained structures and fronts in spatially developing wake flows. *J. Fluid Mech.* **435**, 145–174.

Ponce, V. M. & Simons, D. B. 1977 Shallow wave propagation in open channel flow. *J. Hydr. Div.* **103**, 1461–1476.

Pope, S. B. 2000 *Turbulent Flows*. Cambridge University Press.

van Prooijen, B. C. & Uijttewaal, W. S. J. 2002 A linear approach for the evolution of coherent structures in shallow mixing layers. *Phys. Fluids* **14**, 4105–4114.

Reitz, R. D. 1981 One dimensional compressible gas dynamics calculations using the Boltzmann equations. *J. Comput. Phys.* **42**, 108–123.

Rothman, D. H. 1988 Cellular-automaton fluids: a model for flow in porous media. *Geophysics.* **53**, 509–18.

Schär, C. & Smith, R. B. 1993 Shallow-water flow past isolated topography. Part II: Transition to vortex shedding. *J. Atmos. Sci.* **50**, 1401–1412.

Schlichting, H. 1979 *Boundary-layer Theory*. McGraw-Hill.

Singh, V. P. 1996 *Kinematic Wave Modeling in Water Resources*. Wiley.

Socolofsky, S. A., von Carmer, C. & Jirka, G. H. 2003 Shallow turbulent wakes: Linear stability analysis compared to experimental data. In *Proc. Intl Symposium on Shallow Flows, Delft*, vol. 1, pp. 133–140.

Stansby, P. K. 2003 A mixing-length model for shallow turbulent wakes. *J. Fluid Mech.* **495**, 369–384.

Stansby, P. K. & Lloyd, P. M. 2001 Wake formation around islands in oscillatory laminar shallow-water flows. Part 2. Boundary-layer modelling. *J. Fluid Mech.* **429**, 239–254.

Su, M., Xu, K. & Ghidaoui, M. S. 1999 Low speed flow simulation by the Gas-kinetic scheme. *J. Comput. Phys.* **150**, 17–39.

Tachie, M. F. & Balachandar, R. 2001 Shallow wakes generated on smooth and rough surfaces. *Exps. Fluids* **30**, 467–474.

Uijttewaal, W. S. J. & Booij, R. 2000 Effects of shallowness on the development of free–surface mixing layers. *Phys. Fluids* **12**, 392–402.

Uijttewaal, W. S. J. & Jirka, G. H. 2003 Grid turbulence in shallow flows. *J. Fluid Mech.* **489**, 325–344.

Van Dyke, M. 1982 *An Album of Fluid Motion*. The Parabolic Press. CA.

Wolanski, E. J., Imberger, J. & Heron, M. L. 1984 Island wakes in shallow coastal waters. *J. Geophys. Res.* **89**, 10553–10569.

Xu, K. 1997*a* BGK-based scheme for multicomponent flow calculations. *J. Comput. Phys.* **134**, 122–133.

Xu, K. 1997*b* A gas-kinetic scheme for the Euler equations with heat transfer. *Proc. Intl Symposium on Comput. Fluid Dyn., Beijing*, pp. 247–252. Academic.

Xu, K. 2001 A gas-kinetic BGK scheme for the Navier–Stokes equations and its connection with artificial dissipation and Godunov method. *J. Comput. Phys.* **171**, 289–335.

Xu, K. 2002 A well-balanced gas-kinetic scheme for the shallow-water equations with source terms. *J. Comput. Phys.* **178**, 533–562.

Zhou, J. G. 2004 *Lattice Boltzmann Methods for Shallow Water Flows*. Springer.